

# THE HYDRODYNAMIC FEEDBACK OF COSMIC REIONIZATION ON SMALL-SCALE STRUCTURES AND ITS IMPACT ON PHOTON CONSUMPTION DURING THE EPOCH OF REIONIZATION

HYUNBAE PARK <sup>1,2</sup>, PAUL R. SHAPIRO<sup>1</sup>, JUN-HWAN CHOI<sup>1</sup>, NAOKI YOSHIDA<sup>3,4</sup>, SHINGO HIRANO<sup>3</sup>, AND KYUNGJIN AHN<sup>5</sup>

<sup>1</sup>Texas Cosmology Center and the Department of Astronomy, The University of Texas at Austin, 1 University Station, C1400, Austin, TX 78712, USA

<sup>2</sup>Korea Astronomy and Space Science Institute, Daejeon 34055, Korea

<sup>3</sup>Department of Physics, University of Tokyo, Bunkyo, Tokyo 113-0033, Japan

<sup>4</sup>Kavli Institute for the Physics and Mathematics of the Universe (WPI), Institutes for Advanced Study, University of Tokyo, Kashiwa, Chiba 277-8583, Japan and

<sup>5</sup>Department of Earth Sciences, Chosun University, Gwangju 61452, Korea

(Dated: March 22, 2022)

*Draft version March 22, 2022*

## ABSTRACT

Density inhomogeneity in the intergalactic medium (IGM) on sub-Mpc scales can boost the recombination rate of ionized gas substantially, affecting the growth of H II regions during the Epoch of Reionization (EoR). Previous attempts to express this in terms of a clumping factor,  $C$ , typically failed to resolve the full range of mass and length scales which are important in establishing this effect, down to the Jeans scale in the pre-ionization IGM, along with the hydrodynamical back-reaction of reionization on it. Towards that end, we introduce GADGET-RT, a GADGET code with a new algorithm to transfer H-ionizing radiation, and perform a set of fully-coupled, radiation-hydrodynamics simulations from cosmological initial conditions. We extend the mass resolution of previous work to the scale of minihalos (with masses below  $10^8$  solar masses and virial temperatures below  $10^4$  K), simulating sub-Mpc volumes. Pre-reionization structure is evolved until a redshift  $z_i$  at which the ionizing radiation from external sources during the EoR arrives to sweep an R-type ionization front supersonically across the volume in a few Myr, until it is trapped on the surfaces of minihalos and converted to D-type, after which the minihalo gas is removed by photoevaporative winds. Small-scale density structures during this time lead to a high ( $C > 10$ ) clumping factor for ionized gas. This high clumping factor hugely boosts the recombination rate until the structures are mostly disrupted by the hydrodynamic feedback after  $\sim 10 - 100$  Myr. For incoming stellar radiation with intensity  $J_{21}$ , a number of extra recombinations result per H atom, on top of what is expected from gas at the mean density, is given by  $0.32 [J_{21}]^{0.12} [(1 + z_i)/11]^{-1.7}$ . In models in which most of the volume is ionized toward the end of reionization, this can add up to  $\sim 0.7$  per H atom to the ionizing photon budget to achieve reionization, for patches of the IGM that are close to the mean density when averaged over the patch. We provide fitting functions for the extra recombination rate and mean free path to the ionizing radiation for this case. Even more recombinations and a larger clumping factor will result when full account is also taken of the matter density inhomogeneity on scales larger than that of our sub-Mpc simulation volumes, by including sub-Mpc volumes which depart from the mean density because of large-scale structure formation, as well.

## 1. INTRODUCTION

With growing computational power, simulations of structure formation and radiative transfer are becoming more and more sophisticated in modeling the details of the epoch of reionization (EoR) when the early galaxies led to the ionization of hydrogen in the intergalactic space during the first billion years after the Big Bang (for reviews, see Fan et al. 2006; Robertson et al. 2010). One of the ultimate goals of such simulations is to provide model predictions for observables like 21-cm brightness fluctuations (Paciga et al. 2013; Ali et al. 2015; Asad et al. 2015), secondary CMB anisotropies (George et al. 2015), and the luminosity function of Lyman- $\alpha$  emitters at high redshifts (Krug et al. 2012) that will help to constrain models of EoR via comparison with observational constraints.

A distinctive feature observed on large scales during the EoR is the giant H II regions of ionization growing up to tens of Mpc until they overlap to finish reionization (Barkana & Loeb 2004; Furlanetto et al. 2004; Iliev

et al. 2014). The 21cm signal that directly maps the ionization feature was shown to converge in volumes greater than  $\sim 200 h^{-1}$  Mpc in a side (Iliev et al. 2014). When such a large simulation volume is used, it is usually not computationally feasible to resolve all the baryonic processes related to reionization. Therefore, one has to, for example, rely on sub-grid prescriptions calibrated from small-volume high-resolution simulations accounting for relevant physics. Such an attempt was realized in a large-box ( $\sim 150$  Mpc) reionization simulation where minihalo sources were implemented by sub-grid physics and was shown to be able to generate a significant number of ionizing photons (Ahn et al. 2012).

While much attention has been paid to implementing the *sources* in simulations, quantitative accounting for the *sinks* still requires more study. When a free electron recombines with an ion not directly to the ground state, but cascading through multiple energy levels, it can end up with multiple photons, none of which are able to ionize other atoms. This Case B recombination rate depends

on the clumpiness of the intergalactic medium (IGM). Due to the two-body nature of the reaction, the rate in fully ionized gas goes as the square of density with a temperature dependent coefficient in fully ionized gas. Numerical simulations would underestimate the rate if there exists unresolved density structures within resolution elements (Haiman et al. 2001; Shapiro et al. 2004; Iliev et al. 2005a). To factorize this unknown boost, the clumping factor is often defined as  $C \equiv \langle n^2 \rangle / \langle n \rangle^2$ , where the bracket denotes the volume average and  $n$  is the density of ionized gas<sup>1</sup>. If the volume average is over all of the space, this yields the global clumping factor  $C_{\text{global}}$ , which can also be written as  $1 + \sigma_i^2$ , when  $\sigma_i$  is the root-mean-square (RMS) density fluctuations of the ionized gas. Since the gas density and ionization state fluctuate substantially on large scales as the universe undergoes “patchy” reionization, it is useful to define a spatially-varying local clumping factor,  $C_{\text{local}}(\vec{x})$ . In this factor, the ionized density and its square are averaged over a finite volume  $V$  centered on some point  $\vec{x}$  in space. We can write this as  $1 + \sigma_{<r}^2(\vec{x})$ , where  $\sigma_{<r}(\vec{x})$  is the RMS of the ionized gas density contrast in the volume  $V$  of radius  $r$ , for the density contrast relative to the average ionized density inside  $V$ .

Note that the clumping factor for the entire universe ( $C_{\text{global}}$ , hereafter) is often quoted to estimate the number of ionizing photons needed to keep the universe ionized (Madau et al. 1999). In simulations,  $C_{\text{global}}$  can be expressed as  $1 + \sigma_{<r}^2 + \sigma_{>r}^2$  where  $\sigma_{>r}$  is the rms of the ionized gas density of all the resolution elements in the entire universe. While simulations spanning hundreds of Mpc would capture most of the large-scale variation that goes into  $\sigma_{>r}^2$ ,  $\sigma_{<r}^2$  could be so significant that simply assuming  $C_{\text{global}} = 1 + \sigma_{>r}^2$  would severely underestimate the clumping factor in those simulations. This can be evidenced by the situation that  $C_{\text{global}}$  fails to converge as the simulation resolution increases (e.g., See Figure 15 of Bauer et al. 2015). An error in  $C_{\text{global}}$  is not easily distinguishable in EOR simulations as its effect is largely degenerate with changing the mean efficiency of ionizing sources (i.e., underestimating  $C_{\text{global}}$  and the source efficiency give similar effects.). But, spatial variation of  $C_{\text{local}}$  across resolution elements may leave an observable impact by affecting the growth of H II regions.

Gaseous density structures on sub-Mpc scales are expected to be subject to various baryonic physics, that requires coupled radiative-transfer and hydrodynamics. A number of numerical works dedicated to this problem (Gnedin & Ostriker 1997; Trac & Cen 2007; Pawlik et al. 2009; Raičević & Theuns 2011; Finlator et al. 2012; Shull et al. 2012; Kaurov & Gnedin 2015; So et al. 2014) adopted  $\sim 10^6 M_{\odot}$  for the mass of the dark matter particle aiming to resolve halos down to  $\sim 10^8 M_{\odot}$  corresponding to the mass of  $\sim 10^4$  K gas. This however neglects structures formed during the pre-ionization phase in unheated IGM including *minihalos*. Although

<sup>1</sup> Strictly, the temperature dependence of the recombination coefficient should also be accounted in the clumping factor to accurately estimate the recombination rate although this is often regarded as a minor effect and ignored in studies. We shall present a definition of  $C$  that takes into account the temperature dependence in Section 3 and the quantitative difference made by it in Section 4.1.

it is expected that the hydrodynamical feedback from ionization would disrupt such structures formed in low temperature, one needs to quantify the net recombination during the disruption. In particular, minihalos above  $\sim 10^6 M_{\odot}$  can host dense gas that is capable of being self-shielded from ionizing radiation for a significant amount of time ( $\gtrsim 10^8$  yr) while recombining up to  $\sim 10$  per H atom (Shapiro et al. 2004; Iliev et al. 2005a). Shapiro et al. (2004) and Iliev et al. (2005b) were the first to address this problem by performing fully-coupled radiation-hydrodynamics simulations of individual minihalo photo-evaporation during the EoR.

Such dense neutral clumps of gas often last until the post-reionization era and are found as Lyman-limit systems (e.g., Storrie-Lombardi et al. 1994; Prochaska et al. 2010, 2015). Recombination within Lyman-limit systems can be interpreted as finite limit in the mean free path of H-ionizing radiation (Miralda-Escudé 2003; Songaila & Cowie 2010), which in turn impedes the growth of HII regions beyond a certain size (Gnedin & Fan 2006; Choudhury et al. 2009; Alvarez & Abel 2012). Implementing the effect of finite mean free path of ionizing photons have been found to change predictions for EoR observables from EoR models substantially (Crociani et al. 2011; Iliev et al. 2014; Shukla et al. 2016).

To this end, Emberson et al. (2013, hereafter ETA13) posed a question of how finely one has to resolve small-scale structures to obtain convergence of the clumping factor and mean free path of ionizing photons. As the preferable resolution, they reported dark matter particle mass of  $50 M_{\odot}$  that would well resolve structures down to  $10^4$  solar masses. With that resolution, ETA13 found a substantially higher clumping factor ( $C_{\text{local}} \gtrsim 10$ ) than in other recent works (Raičević & Theuns 2011; Finlator et al. 2012; Shull et al. 2012; Kaurov & Gnedin 2015; So et al. 2014) that have reported values around 3. Their simulation however was based on post-processed radiative transfer that should be valid only before the hydrodynamic feedback on the structures following the photoheating of gas comes into effect. Their reported value is likely to decrease when the Jeans mass increase after reionization.

The goal of this paper is to model  $C_{\text{local}}$  through simulations that keep track of the hydrodynamic evolution of the gas fully coupled with radiation and that adopt the resolution and methodology similar to those suggested by ETA13. Throughout this paper, the background cosmology is based on the Planck cosmology ( $\Omega_M = 0.3175$ ,  $\Omega_{\Lambda} = 0.6825$ ,  $\Omega_b = 0.0490$ ,  $h = 0.6711$ ,  $n_s = 0.9624$ ,  $\sigma_8 = 0.8344$ ; Planck Collaboration et al. 2014).

The remainder of the paper is as follows. In Section 2, we introduce our methodology for simulating the hydrodynamic feedback of reionization. In Section 3, we give our formal definition of the clumping factor and related expression that we will use throughout the paper. In Section 4, we present our results. In Section 5, we discuss the effect of finite box size in our results. We summarize and conclude in Section 6.

## 2. METHODOLOGY

### 2.1. Gravity, Hydrodynamics, & Chemistry

For the hydrodynamics, we adopt the smoothed particle hydrodynamics (SPH) code GADGET-3 (Springel

TABLE 1  
SIMULATION PARAMETER & RESULTS

label	Box size (kpc/ $h$ )	# of ptls	$z_i$	$J_{21}$ ( $\Gamma_{-12}$ )	Shielding	Dynamics (cm $^{-3}$ )	$C_r^{\text{peak}}$ <sup>a</sup>	$N_{\text{rec},150}^{\text{add}}$ <sup>b</sup>	$N_{\text{rec},150}^{\text{bg}}$
S_I0_z10	<b>100</b> <sup>c</sup>	<b>2 × 128<sup>3</sup></b>	10	1 (9.2)	on	on	16.7	0.23	0.12
M_I0_z10_NS	200	<b>2 × 256<sup>3</sup></b>	10	1 (9.2)	<b>off</b>	on	-	0.59	0.12
M_I0_z10_ND	200	<b>2 × 256<sup>3</sup></b>	10	1 (9.2)	on	<b>off</b>	26.0	-	-
M_I0_z10	200	<b>2 × 256<sup>3</sup></b>	10	1 (9.2)	on	on	21.0	0.32	0.12
M_I-0.5_z10	200	<b>2 × 256<sup>3</sup></b>	10	<b>0.3 (2.8)</b>	on	on	12.7	0.28	0.13
M_I-1_z10	200	<b>2 × 256<sup>3</sup></b>	10	<b>0.1 (0.92)</b>	on	on	7.5	0.24	0.13
M_I0_z9	200	<b>2 × 256<sup>3</sup></b>	<b>9</b>	1 (9.2)	on	on	28.1	0.37	0.09
M_I0_z8	200	<b>2 × 256<sup>3</sup></b>	<b>8</b>	1 (9.2)	on	on	37.5	0.45	0.07
L_I0_z10	<b>400</b>	<b>2 × 512<sup>3</sup></b>	10	1 (9.2)	on	on	21.4	-	-

<sup>a</sup>Because  $C_r$  in M\_I0\_z10\_NS has a monotonic behavior, the peak value cannot be defined for this case. M\_I0\_z10\_ND also has the same problem, but we list its converging value instead.

<sup>b</sup>M\_I0\_z10\_ND and L\_I0\_z10 are not run down to  $\Delta t = 150$  Myr.

<sup>c</sup>All numbers in boldface denote a deviation from the parameter choice of the standard run, M\_I0\_z10.

et al. 2001; Springel 2005) with non-equilibrium chemistry of 14 primordial species ( $e^-$ ,  $H$ ,  $H^+$ ,  $H^-$ ,  $He$ ,  $He^+$ ,  $He^{++}$ ,  $H_2$ ,  $H_2^+$ ,  $D$ ,  $D^+$ ,  $HD$ ,  $HD^+$ ,  $HD^-$ ) as described by Yoshida et al. (2006, 2007) with updated cooling rates for  $H_2$  and  $HD$  from Galli & Palla (2013). An SPH code like this is suitable for our target problem because it fixes the mass resolution, allowing us to resolve dense structures with a large number of resolution elements. Throughout this paper, the mass resolution is  $9.3 M_\odot$  for baryonic particles and  $51 M_\odot$  for dark matter particles. This resolution was reported to yield converging result for the clumping factor in ETA13. This resolution corresponds to having  $256^3$  particles for each of dark matter and baryon in a cubic volume of  $(200 h^{-1} \text{ kpc})^3$ .

The initial conditions for  $z = 99$  are created by using MUSIC (Hahn & Abel 2011). While we mainly use a  $200 h^{-1} \text{ kpc}$  size box in our analysis, we also use  $100 h^{-1} \text{ kpc}$  and  $400 h^{-1} \text{ kpc}$  boxes to test the results for the finite box size effect. We first evolve the initial conditions down to  $z = 19$  without any background radiation. After  $z = 19$ , we suppress formation of molecular hydrogen by turning on a uniform Lyman-Werner (LW) background. The spectrum of the LW background is set to be a blackbody of a temperature  $T_{\text{bb}} = 100,000 \text{ K}$ , and is truncated above  $\nu = 13.6 \text{ eV}/h_p$ , where  $h_p$  is the Planck constant. The normalization is set by  $J_{21} = 100$  where  $J_{21}$  is the intensity at  $\nu = 13.6 \text{ eV}/h_p$  in the unit of  $10^{-21} \text{ erg cm}^{-2} \text{ s}^{-1} \text{ Hz}^{-1} \text{ sr}^{-1}$ . As reported in Hirano et al. (2015), this strongly prohibits density gas in minihalos from forming  $H_2$  molecules that would allow the gas to radiatively cool and collapse. This represents our target problem, that of a minihalo which has been deactivated in star formation (SF) throughout its history.

With star-formation suppressed, the sample cubic volume with  $200 h^{-1} \text{ kpc}$  in a side is evolved down to  $z = 8$  and the snapshots are saved at  $z = 10, 9$ , and 8. These snapshots are used as the initial conditions for the runs, in which the external ionizing background radiation (EIBR) is turned on at those redshifts. Two other sample cubic volumes with  $400 h^{-1} \text{ kpc}$  and  $100 h^{-1} \text{ kpc}$  in a side are evolved down to  $z = 10$  in the same way. Here the mass of all the halos is well below  $10^8 M_\odot$ , which roughly corresponds to the Jeans mass for 10,000 K. Therefore, we regard all the structures in our simula-

tion as the small-scale structures from the preionization phase that can not form from ionized gas.

## 2.2. Algorithm for External Ionizing Background Radiation

We adopt an uniform and isotropic background for the ionizing radiation. For each particle, the background radiation is shielded by the neighboring particles within a certain distance,  $l_s$ . Each of the neighboring particles is assigned to the closest one of  $\pm x, \pm y$  and  $\pm z$  directions from the target particle to be shielded to calculate the average column densities of neutral hydrogen for these six directions. The column densities are converted to the attenuation fraction for those directions. Figure 1 is a schematic description of how the neighboring particles are assigned to each direction from the target particle. In the left panel, the target particle is located at the left end of the neutral clump and will not be shielded for the radiation coming from the  $-x$  direction. On the contrary, the target particle in the right panel will be shielded in all of  $\pm x, y$  directions ( $\pm z$  directions are omitted in this description) and it will thus remain completely shielded from the radiation until ionization of outer particles eventually expose it to the radiation.

For each neighboring particle shielding the target particle, we add  $f_{\text{HI}}(m_{\text{gas}}/m_p)/(4\pi d_{\text{sh}}^2/6)$  to HI column density for the direction that the particle is assigned to. Here  $m_{\text{gas}}$ ,  $m_p$ ,  $f_{\text{HI}}$ , and  $d_{\text{sh}}$  are the mass of gas particle, proton mass, the number fraction of hydrogen atom to the number of nucleons and the distance from the shielding particle to the target (shielded) particle, respectively. We assume the neutral fraction of helium follows that of hydrogen and it is only singly ionized when hydrogen is ionized. This is a reasonable assumption for the soft UV spectrum responsible for reionization (Ciardi et al. 2012). This algorithm is implemented into the GADGET-3 code to be directly coupled with the gravity, hydrodynamics, and chemistry solvers. We shall call this code GADGET-RT in this work. Our shielding algorithm is similar to the TreeCol algorithm introduced by Clark et al. (2012). There they segmented the sky seen by the target particle using the HEALPix algorithm (Górski et al. 2005). We test how accurately this code can keep track of photo-evaporation of a spherical minihalo in Appendix A.

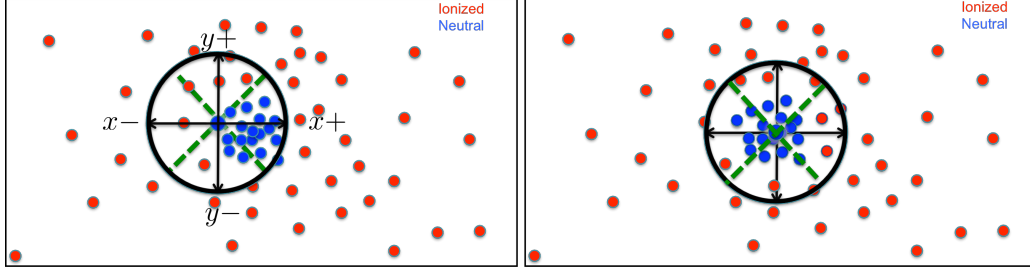


FIG. 1.— (left) A schematic description for the shielding algorithm used in this work. Blue circles denote neutral SPH particles self-shielded from EIBR whereas red circles denote ionized SPH particles. The blue circle at the center of the black circle represents the target particle that we shall calculate the optical depth to EIBR. In this panel a particle at the outer edge of the clump is chosen as the target. The black circle represents the range within which neighboring particles are allowed to shield target particle. Arrows denote  $\pm x, y$  directions on the  $xy$ -plane that we calculate the optical depth separately. The green dashed lines represent the boundary for each direction. (right) Same as the left panel, but the target particle is located at the center of the clump.

### 2.3. Simulations

We simulate the external ionizing background radiation (EIBR, hereafter) using the snapshot outputs described in Section 2.1 as the initial conditions. In the left seven columns of Table 1, we list the name and the parameters of each run. In all the nine simulations, the spectrum of the EIBR is given by the blackbody temperature of  $T_{\text{bb}} = 100,000$  K with the intensity set by  $J_{21} = 1, 0.3$ , or  $0.1$ . Note that this is similar to how we set the LW background in Section 2.1 except that we do *not* truncate the spectrum above  $\nu = 13.6$  eV/ $h_p$ . We adopt M\_I0\_z10, which we use  $J_{21} = 1$  and  $z_i = 10$  as the standard run and create other cases by changing one of the parameters to explore the dependency of the results on each parameter.

For S\_I0\_z10 and L\_I0\_z10, we use  $100 h^{-1}$  kpc and  $400 h^{-1}$  kpc boxes, respectively, to check the convergence of our results for the box size (See Sec. 5). Their initial conditions are from different initializations than those used for M\_I0\_z10. For M\_I0\_z8 and M\_I0\_z9, we set  $z_i = 8$  and  $9$ , respectively, to study the dependence of the results on the timing of reionization. We study the dependence of the results on  $J_{21}$  by changing it to  $0.3$  (M\_I-0.5\_z10) and  $0.1$  (M\_I-1\_z10). We turn off the shielding algorithm for M\_I0\_z10\_NS and disable the dynamics of particles (i.e. freeze particle positions as in post-processed radiative-transfer simulations) for M\_I0\_z10\_ND.

### 3. CLUMPING FACTOR : DEFINITION AND HOW TO CALCULATE

The difference in the ionization rate and recombination rate of hydrogen leads to a change in the number density of ionized hydrogen:

$$\frac{dn_{\text{HII}}}{dt} = \mathcal{I} - \mathcal{R}. \quad (1)$$

The ionization rate can be written as

$$\mathcal{I} \equiv n_{\text{HI}} \int d\Omega \int d\nu \sigma(\nu) \frac{J_{\gamma}(\hat{\Omega}, \nu)}{h\nu}, \quad (2)$$

where  $J_{\gamma}$  is the intensity of the ionizing radiation. And, the recombination rate can be written as

$$\mathcal{R} \equiv \alpha_B(T) n_e n_{\text{HII}}, \quad (3)$$

where  $\alpha_B = 2.6 \times 10^{-13} (T/10^4 \text{ K})^{-0.7} \text{ s}^{-1} \text{ cm}^3$  is the case B recombination coefficient,  $T$  is the gas temperature,

and  $n_X$  denotes the number density of a species  $X$ .

For a resolution element like a pixel in numerical simulations, one can assume the number density of each species and the temperature is uniform within each resolution element when estimating the recombination rate within each resolution element. In that case, the recombination rate can be expressed in terms of the average values of the physical quantities:

$$\bar{\mathcal{R}} = \alpha_B(\bar{T}) \bar{n}_e \bar{n}_{\text{HII}}. \quad (4)$$

Here  $\bar{\mathcal{R}}$ ,  $\bar{n}_e$ , and  $\bar{n}_{\text{HII}}$  are given by the volume average,  $\langle \rangle_V$ . And, the average temperature is given by

$$\bar{T} = (m_p/k_B) \langle (\gamma - 1)u \rangle_M \langle \mu^{-1} \rangle_M^{-1}, \quad (5)$$

where  $u$  is the specific internal energy,  $\mu$  is the mean molecular weight, and  $\langle \rangle_M$  denotes the mass average.

Equation (4) however is not accurate when there are unresolved density/temperature fluctuations within the resolution element. So the clumping factor ( $C$ ) is multiplied to the right-hand-side of Equation (4) to correct for the error. For computational convenience, some works (ETA13, for example) set  $n_e = 1.08 n_{\text{HII}}$  assuming that helium is singly ionized when hydrogen is ionized, and the gas temperature to be constant at 20,000 K or similar. Then, the clumping factor is

$$C_i \equiv \frac{\langle n_{\text{HII}}^2 \rangle_V}{\langle n_{\text{HII}} \rangle_V^2}. \quad (6)$$

And, the recombination rate is

$$\mathcal{R} = C_i \alpha_B(\bar{T}) \bar{n}_e \bar{n}_{\text{HII}} = C_i \alpha_B(T) (1 + \chi) \bar{\chi}^2 \bar{n}_H^2, \quad (7)$$

where  $\chi \equiv n_{\text{HII}}/n_H$  is the ionized fraction of hydrogen.

In this work,  $T$  and  $n_e$  are explicitly computed in the simulations. We can therefore define  $C_r$  in the following way to describe the recombination rate accurately:

$$C_r \equiv \frac{\langle \alpha_B(T) n_e n_{\text{HII}} \rangle_V}{\langle n_{\text{HII}} \rangle_V \langle n_e \rangle_V \alpha_B(\bar{T})}. \quad (8)$$

To define the SPH smoothed field of a physical quantity  $X(\mathbf{r})$  from particle values of  $X$ , we adopt a standard method in SPH:

$$X(\mathbf{r}) = \sum_i \frac{X_i}{n_i} W(\mathbf{r} - \mathbf{r}_i; h_i), \quad (9)$$

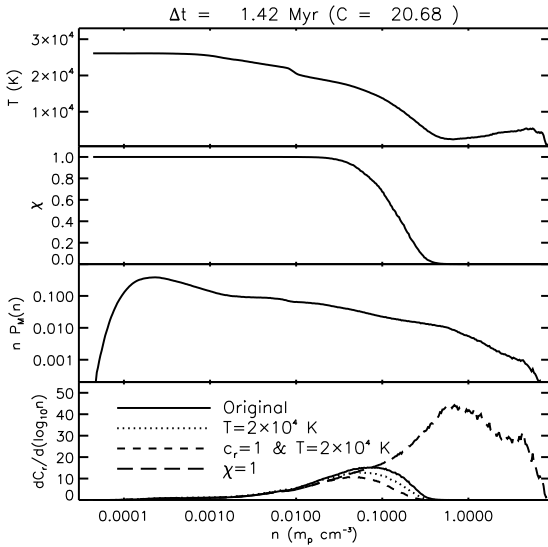


FIG. 2.— The mean gas temperature ( $T$ , top panel), mean ionized fraction ( $\chi$ , upper-middle panel), probability density function ( $P_M$ , lower-middle panel), and clumping factor contribution ( $dC_r/d\log_{10} n$ , bottom panel) as functions of density ( $n$ ) at  $\Delta t = 1.42$  Myr. In the bottom panel, we display a case that we assume a constant temperature  $T = 20,000$  K (dotted line), a case that we assume  $c_r = 1$  as well as  $T = 20,000$  K (dashed line), and a case that we assume complete ionization ( $\chi = 1$ , long dashed line). The areas under the curves in the bottom panel are proportional to the clumping factor expected for the corresponding cases.

where the subscript  $i$  denotes the  $i$ th SPH particle in the simulation,  $n \equiv \rho/m_p$  is the density in the unit of the proton mass  $m_p$ ,  $\mathbf{r}$  is the location,  $W$  is the kernel, and  $h_i$  is the adaptive kernel size given by the distance to the 32nd nearest neighbor from the particle. Then, the volume average of this quantity over the simulation volume  $V_{\text{sim}}$  is given by

$$\langle X \rangle_V = \frac{1}{V_{\text{sim}}} \sum_i \frac{X_i}{n_i} \int_V W(\mathbf{r} - \mathbf{r}_i; h_i) d^3 r. \quad (10)$$

By definition, the volume integral of the kernel in the above should give unity, giving

$$\langle X \rangle_V = \frac{1}{V_{\text{sim}}} \sum_i X_i n_i^{-1}. \quad (11)$$

This allows us to calculate  $C_i$  and  $C_r$  the following summations.

$$C_i = \bar{n}^{-1} N_{\text{ptl}} \left[ \frac{\sum_i n_i \chi_i^2}{(\sum_i \chi_i)^2} \right], \quad (12)$$

$$C_r = \bar{n}^{-1} N_{\text{ptl}} \left[ \frac{\sum_i f_{e,i} f_{\text{HII},i} \alpha_B(T_i) n_i}{(\sum_i f_{e,i}) (\sum_i f_{\text{HII},i}) \alpha_B(\bar{T})} \right]. \quad (13)$$

Here  $N_{\text{ptl}}$  is the number of SPH particles,  $f_X \equiv n_X/n$  is the number density of a species  $X$  divided by  $n$ , and  $\bar{T}$  is given by averaging over the particle values:  $N_{\text{ptl}}^{-1} \sum_i T_i$ .

Both  $C_i$  and  $C_r$  are calculable from our simulations, but using  $C_r$  should give the accurate recombination rate. Thus, we by default refer to  $C_r$  when we mention the clumping factor in the rest of this paper. And, we shall

give the value of  $C_i$  where we look into the the difference between  $C_r$  and  $C_i$  such as in Section 4.1.

We also express Equations (12) and (13) as the integrals over  $n$  to describe the clumping factor contribution from gas with a certain density. This is done by using a combination of relevant physical quantities ( $\chi$ ,  $f_e$  &  $T$ ) averaged at a given  $n$  and the mass-weighted probability density function (PDF) for SPH particles,  $P_M(n') = dN_{\text{ptl}}/dn'^2$ :

$$C_i = \frac{\int dn' P_M(n') \chi(n')^2 c_i(n') n'}{\bar{n} \langle \chi \rangle_M^2} \quad (14)$$

$$C_r = \frac{\int dn' P_M(n') \chi(n') f_e(n') \alpha_B(T(n')) c_r(n') n'}{\bar{n} \langle \chi \rangle_M \langle f_e \rangle_M \alpha_B(\bar{T})}. \quad (15)$$

Here the mass average of a quantity  $\langle X \rangle_M$  is given by  $N_{\text{ptl}}^{-1} \sum_i X_i$ . To obtain physical quantities as functions of  $n$  (e.g.,  $\chi(n)$ ), we place all the SPH particles onto, 400 logarithmically uniform bins between the maximum and minimum densities, and calculate the average value for each quantity. In addition, we define clumping factors sampled at density  $n'$ :

$$c_i(n') \equiv \frac{\langle \chi^2 \rangle_{n=n'}}{\bar{\chi}(n')^2}; \quad c_r(n') \equiv \frac{\langle \chi f_e \alpha_B(T) \rangle_{n=n'}}{\bar{\chi}(n') \bar{f}_e(n') \alpha_B(\bar{T}(n'))}$$

where the bracket  $\langle \cdot \rangle_{n=n'}$  denotes a mass average within the bin for  $n = n'$  that we calculate other physical quantities. These factors arise due to variations in the physical quantities at a given density. They should be included in the integral to precisely recover  $C_i$  and  $C_r$  calculated from Equations (12) and (13), respectively. We shall describe how each physical quantity affects the clumping factor using the integral form more specifically in Section 4.1.

#### 4. RESULTS

The main results of this paper are summarized in this section.

##### 4.1. Physical Quantities Relevant to Clumping Factor

In Equations (14) and (15), we express the clumping factor in terms  $\chi$ ,  $P_M$ ,  $f_e$ , and  $T$  as functions of  $n$ . In this section, we point out that the  $n$ -dependence of  $dC_r/d\log_{10} n$  (the integrand of Eq. 15) is practically dictated by  $\chi$  and  $P_M$  going as  $n^2 \chi^2 P_M$ . Then, we shall focus on  $\chi$  and  $P_M$  as functions of  $n$  to understand the time evolution of the clumping factor in the rest of this paper.

We plot  $\chi$ ,  $P_M$ ,  $T$ , and  $dC_r/d\log_{10} n$  are plotted as functions of  $n$  in Figure 2 for the snapshot of M\_I0\_z10 at  $\Delta t = 1.42$  Myr.  $f_e$  is found to be close to  $0.82\chi$ , which is consistent helium singly-ionized with hydrogen throughout our analysis, and we do not plot it in this paper. Due to shielding against the EIBR, a break appears in  $\chi$  at a certain  $n$ , above which  $\chi$  falls to zero. At  $n \lesssim 0.3 \text{ cm}^{-3}$  where the gas is at least partially ionized ( $\chi > 0$ ), the

<sup>2</sup> The volumed weighted gas density PDF of Miralda-Escudé et al. (2000) is related to our mass-weighted density PDF by  $\Delta P_V(\Delta) d\Delta = P_M(n) dn$ , where  $\Delta = n/\bar{n}$  is the normalized density.

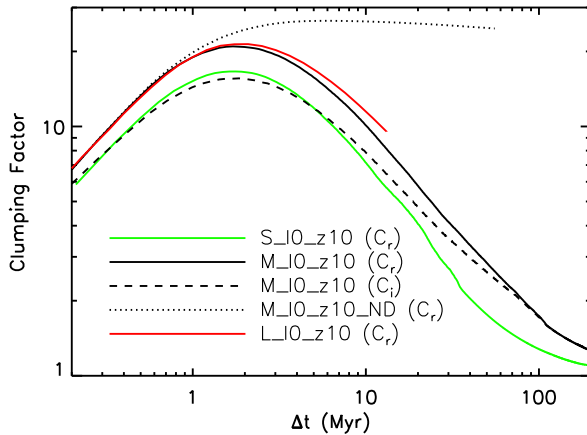


FIG. 3.— The clumping factor plotted as a function of time for several different cases. The solid lines compare  $C_r$  from simulations with different box sizes, S\_I0\_z10 (green), M\_I0\_z10 (black), and L\_I0\_z10 (red). The dotted black line denotes  $C_r$  from M\_I0\_z10\_NS to verify the impact of shielding. Finally, the black dashed line is  $C_r$  from M\_I0\_z10.

gas temperature tends to anti-correlate with the density.  $P_M$  is nearly unchanged from the initial conditions at the turn-on of EIBR. It shows a gaussian-like distribution around the cosmic mean ( $n = 3.3 \times 10^{-4} \text{ cm}^{-3}$ ) with an extended power-law-like tail between  $n \approx 10^{-3}$  and  $5 \times 10^{-1} \text{ cm}^{-3}$  with the power-law index of -1.5. Then, it falls off faster above  $n \sim 5 \times 10^{-1} \text{ cm}^{-3}$ . This behavior is consistent with what is reported in Miralda-Escudé et al. (2000).

To assess the impact of each term, we create the following three hypothetical cases and plot  $dC_r/d\log_{10} n$  for those cases in the bottom panel of Figure 2.

Case 1: Assume a constant temperature  $T = 20,000 \text{ K}$ . In this case,  $C_r$  becomes  $C_i$ .

Case 2: Ignore  $c_r$  by setting it to unity as well as assuming  $T = 20,000 \text{ K}$ . This makes  $dC_r/d\log_{10} n$  goes precisely as  $n^2 \chi^2 P_M$ .

Case 3: Assume complete ionization by setting  $\chi = 1$ .

Case 1 and Case 2 mostly reproduce the shape of  $dC_r/d\log_{10} n$  with a moderate underestimation at  $n \gtrsim 10^{-2} \text{ cm}^{-3}$ .  $dC_r/d\log_{10} n$ , which is roughly proportional to  $n^{0.5}$  up to  $n \approx 3 \times 10^{-2} \text{ cm}^{-3}$ , where  $\chi$  is almost unity and the  $n^2 P_M$  term determines its behavior. At above  $n \approx 3 \times 10^{-2} \text{ cm}^{-3}$ , the break in  $\chi$  suppresses  $dC_r/d\log_{10} n$ .

Around the break,  $dC_r/d\log_{10} n$  in Case 1 and Case 2 is lower then that in the original case due the effect of the gas temperature. The actual gas temperature falls toward the high- $n$  direction intersecting 20,000 K at  $n \approx 10^{-2} \text{ cm}^{-3}$ . The recombination coefficient has goes as  $T^{-0.7}$  and it therefore decreases with increasing density. So,  $\alpha_B(T)$  is underestimated at  $n \gtrsim 10^{-2} \text{ cm}^{-3}$  and is overestimated at  $n \lesssim 10^{-2} \text{ cm}^{-3}$  when assuming  $T = 20,000 \text{ K}$ . Nevertheless, only the underestimation stands out because  $dC_r/d\log_{10} n$  practically vanishes at  $n \lesssim 10^{-2} \text{ cm}^{-3}$  due to its  $n^{0.5}$  scaling. Assuming  $c_r = 1$  causes an additional underestimation at

$n \gtrsim 3 \times 10^{-2} \text{ cm}^{-3}$  in Case 2. In that density, the gas is partially ionized and  $\chi$ ,  $f_e$ , and  $\alpha_B(T)$  has scatters giving  $c_r > 1$ .

The break in  $\chi$  is an important consequence of the shielding mechanism. Case 3 shows how drastically the clumping factor would be overestimated without the break.  $dC_r/d\log_{10} n$  keeps rising as  $n^{0.5}$  up to  $n \sim 1 \text{ cm}^{-3}$  in that case. The resulting clumping factor is about 70 much higher than the actual clumping factor 20.

Case 1 corresponds to using  $C_i$  for the clumping factor as in most previous literature that did not keep track of the gas temperature. Despite the impact of the gas temperature on the clumping factor is relatively minor compared to those of  $\chi$  and  $P_M$ , it still matters when it comes to estimating the recombination rate precisely. The time evolutions of  $C_i$  and  $C_r$  are compared in Figure 3. The difference peaks at  $\Delta t = 1.42 \text{ Myr}$ , where  $C_i$  is about 16 and  $C_r = 21$ . Then, they converge to each other as they decay toward unity altogether at  $\Delta t \gtrsim 10 \text{ Myr}$ .

#### 4.2. Time Evolution of the Clumping Factor: Dual Phase Evolution

The clumping factor as a function of time is shown for each model in Figure 3 and in the left panel of Figure 4. Except for the runs without shielding (M\_I0\_z10\_NS) or dynamics (M\_I0\_z10\_ND), we find that the clumping factor starts rising in the early time, turns over at  $\Delta t = 1 - 3 \text{ Myr}$ , and falls afterwards eventually converging to unity at  $\Delta t \gtrsim 100 \text{ Myr}$ . We explain this behavior with the two phases of ionization fronts (I-fronts) in the following and shall look into the standard run (M\_I0\_z10) as the main sample for this discussion.

**1. R-type:** I-fronts propagate super-sonically through low density IGM. They sweep gaseous structures without giving enough time to react to ionization.

**2. D-type:** As I-fronts reach dense regions, they become sub-sonic and can no longer proceed before the hydrodynamic feedback begins to move the gas. The gas expands due to increased pressure from photo-ionization substantially with the I-fronts.

The simulation starts with R-type I-fronts in low density regions. As I-fronts progress super-sonically toward density peaks, neutral regions shrink while the density field remains nearly unchanged. A schematic description is shown in the column density maps in Figure 5 for the snapshots at  $\Delta t = 0.14 \text{ Myr}$  and  $1.42 \text{ Myr}$ . The ionization profile and density PDF in Figure 6a give more quantitative information. The major change happens in the break of ionization profile that the ionization fraction transitions from ionized to neutral. The break shifts from  $n = 0.03 \text{ cm}^{-3}$  to  $0.2 \text{ cm}^{-3}$  from  $\Delta t = 0.14 \text{ Myr}$  and  $1.42 \text{ Myr}$  while the density PDF remains almost the same. To describe the location of the break, we define  $n_{\text{crit}}$  as the density that  $\chi(n = n_{\text{crit}}) = 0.5$  and show it in Figure 7.  $n_{\text{crit}}$  rises steadily during this time. As  $n_{\text{crit}}$  rises,  $dC_r/d\log_{10} n$  picks up extra contribution from the gas that is newly included in the density range  $n < n_{\text{crit}}$ . Due to the  $\sqrt{n}$  scaling of  $n^2 P_M$ , this adds progressively

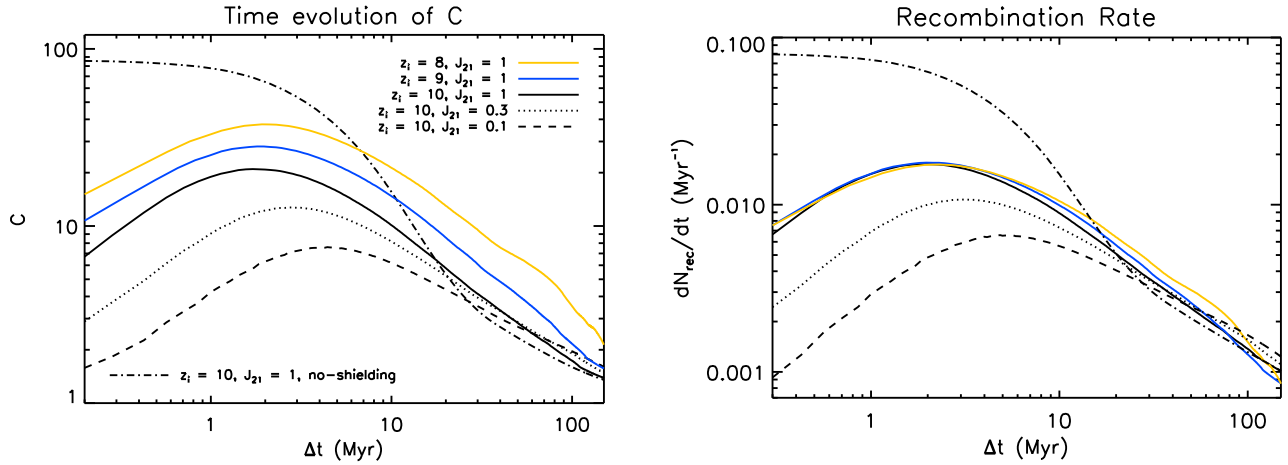


FIG. 4.— (left) The clumping factor as a function of time for M\_I0\_z10 (black solid), M\_I-0.5\_z10 (black dotted), M\_I-1\_z10 (black dashed), M\_I0\_z9 (blue solid), M\_I0\_z8 (yellow solid), and M\_I0\_z10\_NS (black dot-dashed). (right) The recombination rate as a function of time for the same runs used in the left panel.

more to the clumping factor. This is why the clumping factor rises rapidly during the early time.

From  $\Delta t \approx 2$  Myr, the I-fronts in the simulation transition to D-type. Disruption of ionized structures stands out in the column density maps (Fig. 5). Filamentary structures diminish as they expand and dilute with the background.  $n_{\text{crit}}$  in Figure 7 settles down at around  $0.2 \text{ cm}^{-3}$  and no longer evolves substantially<sup>3</sup>. Evaporation keeps going on on the surfaces of neutral clumps reducing the number of the clumps in time. At  $\Delta t = 37$  Myr, most of the structures are gone except for a few clumps that started in the most massive minihalos in the volume. As the hydrodynamical feedback causes the dense ionized gas to expand to lower densities, the density PDF (middle panel of Fig. 6a) at  $n < n_{\text{crit}}$  is suppressed preferentially faster from the high-density side. Since the high-density ionized gas is main source of  $dC_r/d\log_{10} n$  (bottom panel of Fig. 6a), the clumping factor decays with the expansion of that gas.

The density and ionization histories of individual particles support this dual phase picture as well. We sample ten SPH particles with difference initial densities and show how their densities and ionized fractions evolve over time in Figure 8. SPH particles above the asymptotic value of  $n_{\text{crit}}$  ( $0.2 \text{ cm}^{-3}$ ) are ionized by R-type I-fronts shortly and drop in their densities down close to the cosmic mean ( $n_{\text{mean}} = 3.3 \times 10^{-4} \text{ cm}^{-3}$ ). The particles with  $n > 0.2 \text{ cm}^{-3}$  are not ionized immediately due to the shielding. But, they eventually get ionized when exposed to the surface of the clumps they reside, and go through similar density drops from the point of ionization.

#### 4.2.1. Roles of Shielding and Hydrodynamics

The dual phase evolution described above is a consequence of implementing the self-shielding of dense neutral gas while keeping track of the hydrodynamics. To bring out their importance, we run one no-shielding run (M\_I0\_z10\_NS) and one no-dynamics run (M\_I0\_z10\_ND).

<sup>3</sup>  $n_{\text{crit}}$  is shown to rise slightly after  $\Delta t \sim 40$  Myr in the figure. But, this is not a statistically meaningful feature as it is from very little gas left in a single evaporating minihalo.

For the no-shielding run, we simply turn off our shielding algorithm and let all the SPH particles be exposed to the EIBR. In the no-dynamics run, we force particles to stay in their initial locations to mimic post-processed radiative transfer.

Ionization in the no-shielding run happens everywhere at the beginning. I-fronts therefore do not exist in this run. The HI column density map for  $\Delta t = 1.4$  Myr (left panel of Fig. 9) lacks most of the spurious high-column density regions with  $N_{\text{HI}} > 10^{19} \text{ cm}^2$  present in M\_I0\_z10 (top right panel of Fig. 5). Subsequence expansion of gas looks similar, but the no-shielding run lacks self-shielded cores as can be seen for  $\Delta t = 37$  Myr in the right panel of Figure 9. The break in the ionization profile cannot exist in this case because all the gas is nearly fully ionized from the beginning.  $dC_r/d\log_{10} n$  at  $\Delta t = 0.14$  & 1.4 Myr (bottom panel of Fig. 6e) picks up a huge contribution from  $n < n_{\text{crit}}$  similarly to in the  $\chi = 1$  case of the standard run (bottom panel of Fig. 2). Later, the gas with  $n \gtrsim 0.03 \text{ cm}^{-3}$  is totally gone as shown by  $P_M$  at  $\Delta t = 37$  Myr while the standard run retains some amount of self-shielded gas. The clumping factor in the no-shielding run therefore starts much higher ( $\sim 100$ ) than in the standard run. And, it falls below that in the standard run after  $\Delta t \sim 20$  Myr because the no-shielding run lacks self-shielded clumps that contribute to the clumping factor via the newly evaporating gas.

The no-dynamics run, on the other hand, goes similarly to the standard run while I-fronts are in the R-type phase. But, all sorts of evolution stops after  $\Delta t \sim 1$  Myr when I-fronts are supposed to transition to D-type. This is described in the HI column density map (Fig. 10d); the map is nearly unchanged from  $\Delta t = 1.4$  Myr to 37 Myr. The I-fronts become stuck on surfaces of the self-shielded clumps as the gas does not expand to give ways into the clumps. The EIBR reaches a state that it consumes all the photons due to on-going recombination in already ionized gas. The ionization profile (Fig. 6d) stops evolving after  $\Delta t \sim 7.1$  Myr. And, the density PDF stays the same except for a tiny shift toward lower densities due to the Hubble expansion.

The results in this section demonstrate the importance

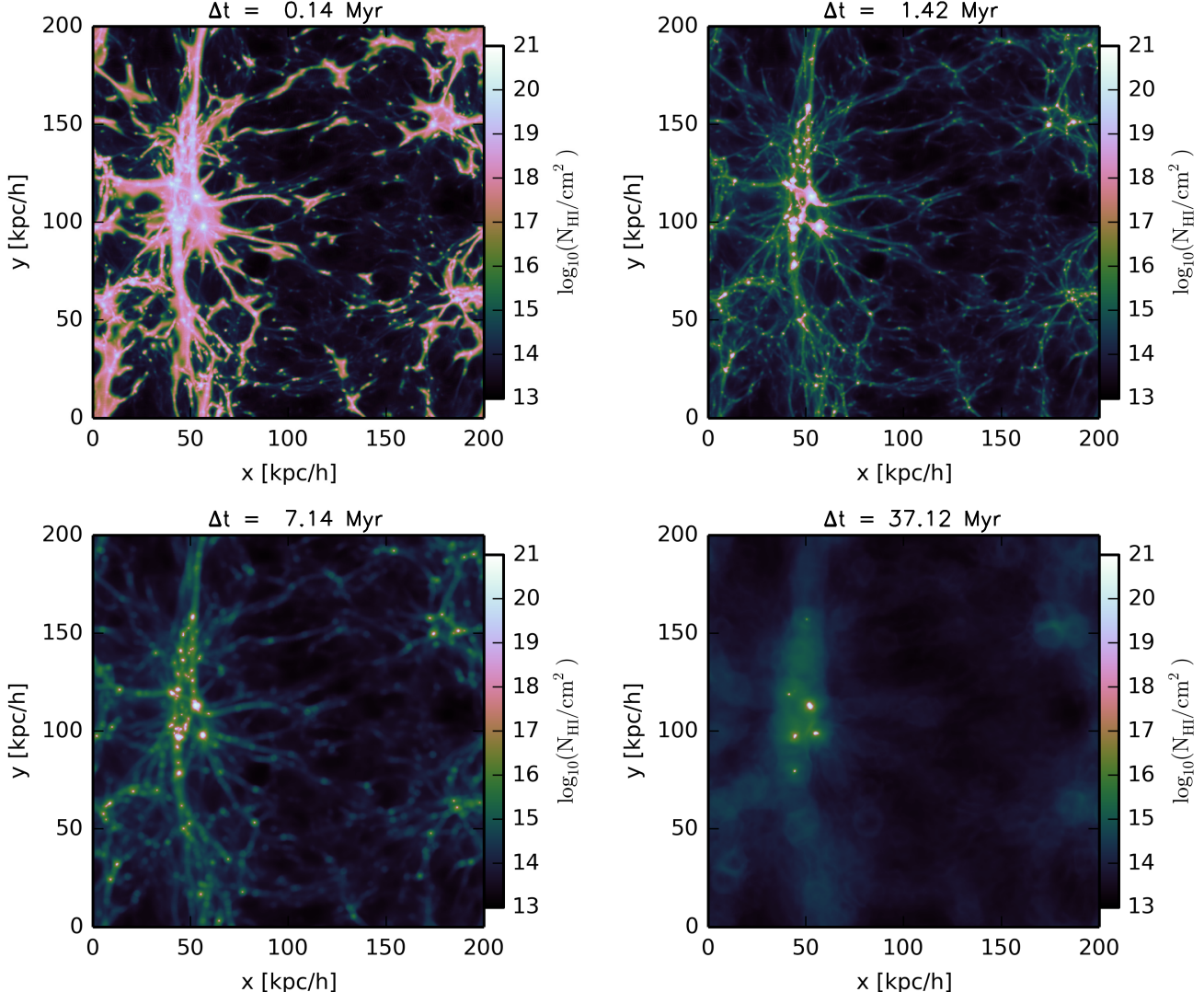


FIG. 5.— The projected neutral column density of M\_I0\_z10 at  $\Delta t = 0.14$  Myr (top left), 1.4 Myr (top right), 7.1 Myr (bottom left), and 37 Myr (bottom right). White and pink colors display the neutral regions, and green and black colors display the ionized regions.

of shielding in reproducing R-type I-fronts in early times, and that of the dynamics in reproducing D-type I-fronts that comes after. Neglecting the former hugely overestimates the clumping factor in the early times by not excluding the self-shielded dense clumps in the calculation. And, neglecting the latter would miss the hydrodynamic evolution of the gas and lead to an overestimation of the clumping factor, which instead would decrease during the formation of the D-type front due to photo-evaporation of gas.

#### 4.3. Parameter Dependence of the Clumping Factor

On large scales, there would be sub-Mpc volumes that are ionized at different times ( $z_i$ ) by EIBR with different intensities ( $J_{21}$ ) than in the standard run due to the variance in their environment. In order to cover all such cases, we create multiple runs, in which we change one of  $J_{21}$  or  $z_i$  from the parameter choice of the standard run ( $z_i = 10$ ;  $J_{21} = 1$ ). We have two runs, M\_I-0.5\_z10 and M\_I-1\_z10, that the EIBR intensities are  $J_{21} = 0.3$  and 0.1, respectively, and other two runs, M\_I0\_z9 and

M\_I0\_z8, that ionizes at  $z_i = 9$  and 8, respectively. The resulting clumping factors are shown in the left panel of Figure 4. While the appearance of both R-type and D-type phases is a generic trend, some details differ amongst the cases.

The lower  $J_{21}$  is, the lower the clumping factor starts and the later it turns over. This is because the I-fronts with a lower intensity propagate more slowly and transition into D-type at a lower density. The column density map of M\_I-1\_z10 at  $\Delta t = 1.42$  Myr in the left panel of Figure 11 shows that the high column density ( $N_{\text{HI}} \gtrsim 10^{19} \text{ cm}^{-2}$ ) regions are more extended than in M\_I0\_z10 (upper right panel of Fig. 5). This denotes a slower progress of ionization in M\_I-1\_z10 than in M\_I0\_z10. At a later time  $\Delta t = 37$  Myr (right panel of Fig. 11), much larger number of neutral clumps are still observed than in the standard run.  $n_{\text{crit}}$  in M\_I-1\_z10 (Fig. 7) asymptotes to  $\sim 0.04 \text{ cm}^{-3}$  that is 5 times lower than it does in the standard run. Also, it reaches to asymptote after  $\sim 10$  Myr, taking about 7 times longer than it does in the standard run (See also the

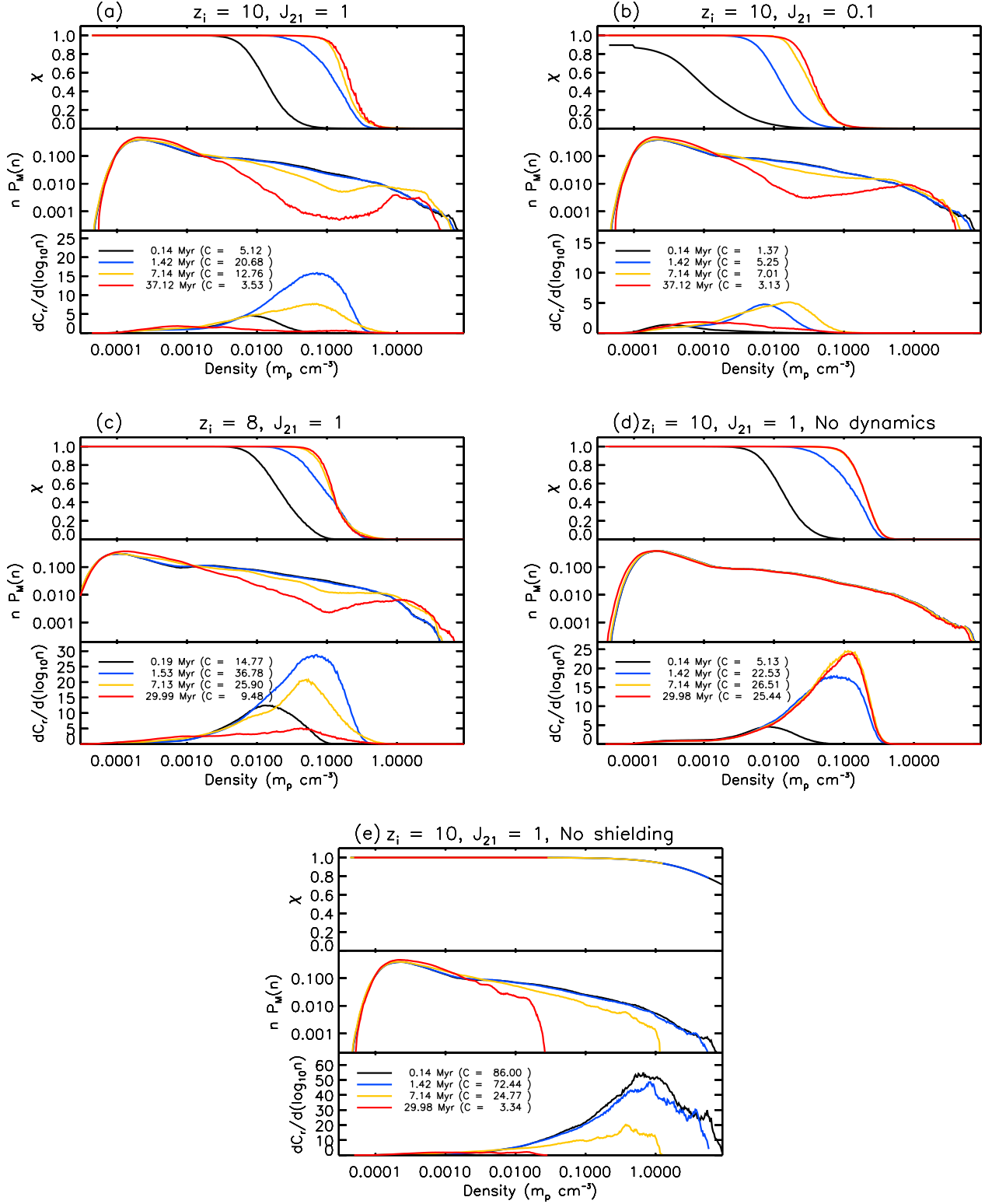


FIG. 6.— The mean ionized fraction ( $\chi$ ), probability density function ( $P_M$ ), and clumping factor contribution ( $dC_r/d\log_{10} n$ ) as functions of  $n$  are plotted in the top, middle, and bottom panels, respectively. The results are shown for M\_I0\_z10 (panel a), M\_I-1\_z10 (panel b), M\_I0\_z8 (panel c), M\_I0\_z10\_ND (panel d), and M\_I0\_z10\_NS (panel e). Except for M\_I0\_z10\_z8, the black, blue, yellow and red lines describe the results at  $\Delta t = 0.14$  Myr, 1.4 Myr, 7.1 Myr, and 30 Myr, respectively. For M\_I0\_z10\_z8, the same colors describe  $\Delta t = 0.19$  Myr, 1.53 Myr, 7.13 Myr, and 30 Myr, respectively.

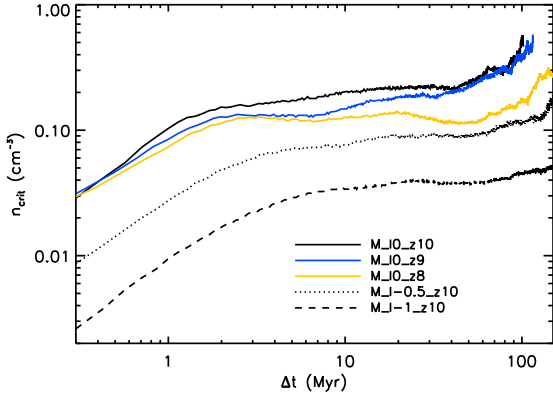


FIG. 7.— The critical density of ionization ( $n_{\text{crit}}$ ) as a function of time from the turn-on of EIBR ( $\Delta t$ ). We show the result for M\_I0\_z10 (black solid), M\_I0\_z9 (blue solid), M\_I0\_z8 (yellow solid), M\_I-0.5\_z10 (black dotted), and M\_I-1\_z10 (black dashed). Above a certain density, all the gas is ionized and  $n_{\text{crit}}$  cannot be defined because  $\chi(n) > 0.5$  for all  $n$ 's. That is where the curve ends for M\_I0\_z10 and M\_I0\_z9. We also advise the reader to be cautious that  $n_{\text{crit}}$  is not statistically reliable near where it is cut because there is very little neutral gas left at those times.

evolution of the ionization profile in the top panel of Fig. 6b). With  $dC_r/d\log_{10} n$  suppressed from a lower density ( $\sim 0.04 \text{ cm}^{-3}$ ), the resulting clumping factor is also lower. The slower evaporation leads to a larger amount of high-density self-shielded gas remaining at late time as can be seen in the density PDF at  $\Delta t = 37 \text{ Myr}$  (middle panel of Fig. 6b). This delay in evaporation makes the clumping factor decay more slowly and eventually it causes M\_I-1\_z10 to have slightly higher clumping factor at around  $\Delta t = 50 \text{ Myr}$  than the standard run does.

When  $z_i$  is lower, the clumping factor evolves similarly to in the standard run, but the overall magnitude is higher by roughly a constant factor (See Fig. 4). The peak clumping factor ( $C_r^{\text{peak}}$ ; listed in Table 1) can be taken as the reference for the relative magnitude of each case, which we find to scale nearly as  $(1+z)^{-3}$ . This is the inverse of what the cosmic mean density does. Here we note that the recombination rate per hydrogen atom,

$$\frac{dN_{\text{rec}}}{dt} \equiv \frac{\langle \mathcal{R} \rangle_V}{f_{\text{H}} \bar{n}} = C_r \frac{\alpha_B(\bar{T}) \bar{n}_{\text{HII}} \bar{n}_e}{f_{\text{H}} \bar{n}}, \quad (16)$$

goes as the *first* power of the cosmic mean density,  $\bar{n}$ , for a fixed  $C_r$  in the fully ionized regime where both  $\bar{n}_{\text{HII}}$  and  $\bar{n}_e$  go as  $\bar{n}$ . Thus,  $C_r$  going as the inverse of  $\bar{n}$  causes the mass-weighted recombination rate to stay fixed for changing redshift.

When we plot  $dN_{\text{rec}}/dt$  directly in the right panel of Figure 4, we find  $dN_{\text{rec}}/dt$  does not change much for changing  $z_i$ . But, it falls more slowly for lower  $z_i$ 's during the D-type phase. The difference in the D-type phase is due to the growth of structures building up more self-shielded gas at lower  $z_i$ . The late time clumping factor in lower  $z_i$  runs has more contribution from evaporating self-shielded clumps.

#### 4.4. Interpretation of the Results of ETA13

ETA13 used their post-processed radiative-transfer simulations to explore the dependence of the clumping

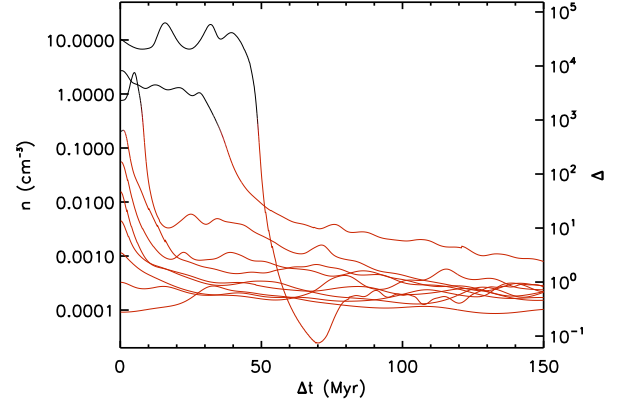


FIG. 8.— The densities of ten SPH particles in M\_I0\_z10 as functions of time. The color represents the ionization status of the particle with the black color meaning that neutral and red ionized.

factor on  $z_i$  and  $\Gamma_{-12}$ . Here

$$\Gamma_{-12} \equiv \left( \frac{0.3}{10^5 \text{ cm}^{-2} \text{ s}^{-1}} \right) \int \Omega \int_{13.6 \text{ eV}}^{54.4 \text{ eV}} \frac{I_\nu}{h\nu} d\nu, \quad (17)$$

where  $I_\nu$  is the intensity of the EIBR at the frequency  $\nu$ . Their main result for the clumping factor is in Figure 4 of their work<sup>4</sup>. Their reported clumping factor was substantially larger than that of the recent works ( $\sim 3$ ) in most of their parameter space. For example, their clumping factor is well above 10 for  $z_i < 10$  and  $\Gamma_{-12} > 1$ . We list  $z_i$  and  $\Gamma_{-12}$  for our simulations in Table 1 to allow reading out their version of the clumping factor.

Our no-dynamics run (M\_I0\_z10\_ND) mimics their methodology by ionizing SPH particles with the particle locations fixed. We suppose the asymptotic state of the no-dynamics run corresponds to the simulation of ETA13. The no-dynamics run uses  $[z_i, \Gamma_{-12}] = [10, 9.2]$  and  $C_r^{\text{peak}}$  asymptotes to 26. Here we note that ETA13 calculated  $C_i$  for the clumping factor. As we find in Section 4.1,  $C_i$  is lower than  $C_r$ . In the asymptotic state of the no-dynamics run, we have  $C_i = 21$  that agrees well with their result.

In other runs that we allow particles to move, the peak clumping factor is comparable to and has a parameter dependence similar to the clumping factor of ETA13. For changing  $z_i$ , M\_I0\_z10, M\_I0\_z9, and M\_I0\_z8 give  $C_r^{\text{peak}} = 21, 28$ , and 38 while ETA13 reports  $C_i = 21, 30$ , and 45, respectively. For changing  $\Gamma_{-12}$ , M\_I0\_z10, M\_I-0.5\_z10, and M\_I-1\_z10 give  $C_r^{\text{peak}} = 21, 13$ , and 8 while ETA13 reports  $C_i = 21, 15$ , and 12, respectively. Noting that  $C_i$  is about 70% of  $C_r$  at the peak,  $C_r^{\text{peak}}$  in these runs seems to be lower by 30 - 50% the result of ETA13. Such discrepancies are expected because the hydrodynamic feedback should decrease the clumping factor in those runs compared to in the no-shielding run.

Overall, the high ( $> 10$ ) clumping factor that ETA13 reported does appear in our simulation when small-scale structures are ionized up to the highest density possible for the EIBR to ionize, but it is still early enough that the

<sup>4</sup> Both left and right panels of the figure give the clumping factor for given  $z_i$  and  $\Gamma_{-12}$ . But, each panel gives a slightly different clumping factor for the parameters of our interest. We shall adopt the left panel in our discussion.

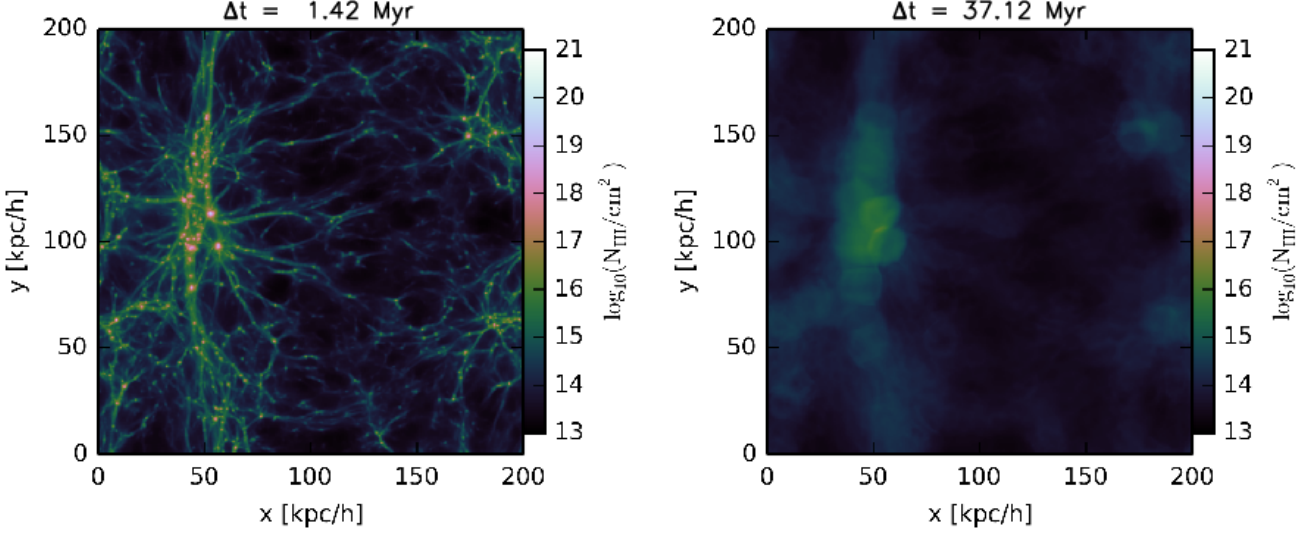


FIG. 9.— The projected H I column density of M\_I0\_z10\_NS at  $\Delta t = 1.4$  Myr (left) and 37 Myr (right).

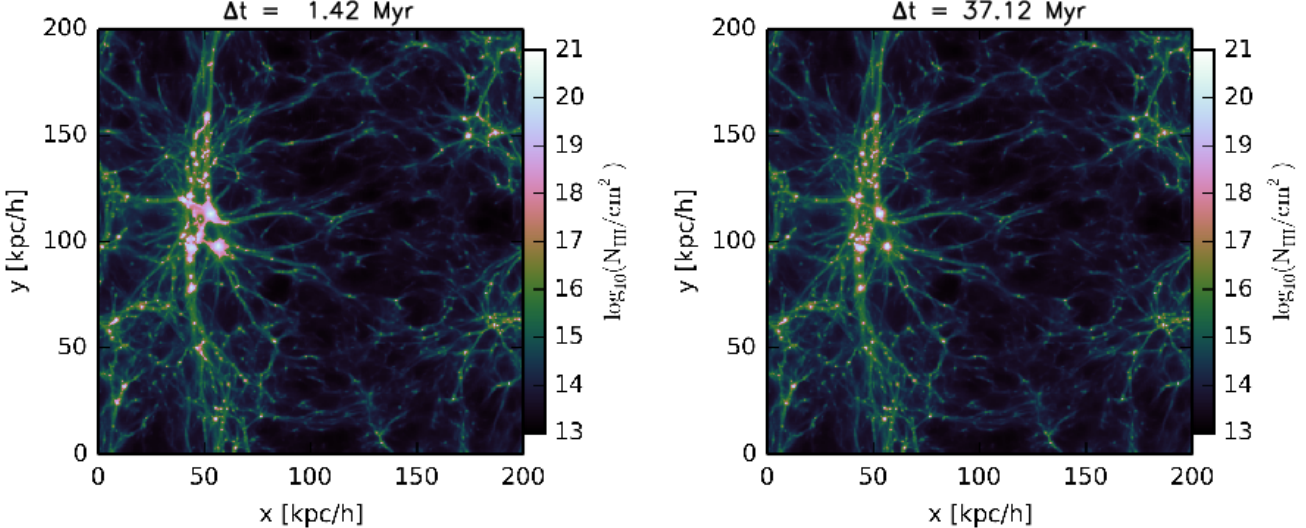


FIG. 10.— The projected H I column density of M\_I0\_z10\_ND at  $\Delta t = 1.4$  Myr (left) and 37 Myr (right).

structures are yet to be disrupted by the hydrodynamic feedback. This however is rather transient phenomenon because the small-scale structures are quickly destroyed due to their increased pressure from photo-ionization.

#### 4.5. Ionizing Photon Budget for Small-scale Structure

To determine the significance of the temporary boost of the clumping factor by small-scale structures, one needs to assess its overall impact on time-integrated quantities. The accumulated recombination per hydrogen atom can be obtained by integrating Equation (16) w.r.t. time:

$$N_{\text{rec}}|_{\Delta t} \equiv \int_{t=0}^{\Delta t} \frac{dN_{\text{rec}}}{dt} dt = \int_{t=0}^{\Delta t} C_r \frac{\alpha_B(\bar{T}) \bar{n}_{\text{HII}} \bar{n}_e}{f_{\text{H}} \bar{n}} dt \quad (18)$$

To separate out the base amount expected from the case that the simulation is homogenous without any structure, we define the “background recombination count” as  $N_{\text{rec}}^{\text{bg}} \equiv C_r^{-1} N_{\text{rec}}$ . Then, the rest,  $N_{\text{rec}}^{\text{add}} \equiv (1 - C_r^{-1}) N_{\text{rec}}$ ,

can be interpreted as the additional from the structures on top of the background. We plot  $N_{\text{rec}}$  and  $N_{\text{rec}}^{\text{bg}}$  as functions of time for M\_I0\_z10, M\_I0\_z9, M\_I0\_z8, M\_I-0.5\_z10, M\_I-1\_z10, and M\_I0\_z10\_NS in Figure 13. In this case,  $C_r$  is the ratio of the slope of  $N_{\text{rec}}$  to that of  $N_{\text{rec}}^{\text{bg}}$ .

Up to  $\Delta t \lesssim 20$  Myr, the boost in the clumping factor makes  $N_{\text{rec}}$  accumulate much faster than  $N_{\text{rec}}^{\text{bg}}$  does. Later ( $\Delta t \gtrsim 20$  Myr), the slope of  $N_{\text{rec}}$  asymptotes to that of  $N_{\text{rec}}^{\text{bg}}$  as  $C_r$  decays toward unity. As a result,  $N_{\text{rec}}$  minus  $N_{\text{rec}}^{\text{bg}}$  becomes nearly a fixed quantity after  $\Delta t = 150$  Myr. Thus, we interpret  $N_{\text{rec},150}^{\text{add}} \equiv N_{\text{rec}}^{\text{add}}|_{\Delta t=150 \text{ Myr}}$  as the *ionizing photon budget for the pre-ionization IGM*. We list  $N_{\text{rec},150}^{\text{add}}$  and  $N_{\text{rec},150}^{\text{bg}} \equiv N_{\text{rec}}^{\text{bg}}|_{\Delta t=150 \text{ Myr}}$  in Table 1 for each run. Note that  $N_{\text{rec},150}^{\text{bg}}$  is not a fixed quantity but grows in time.

Similarly to the peak clumping factor,  $N_{\text{rec},150}^{\text{add}}$  is larger

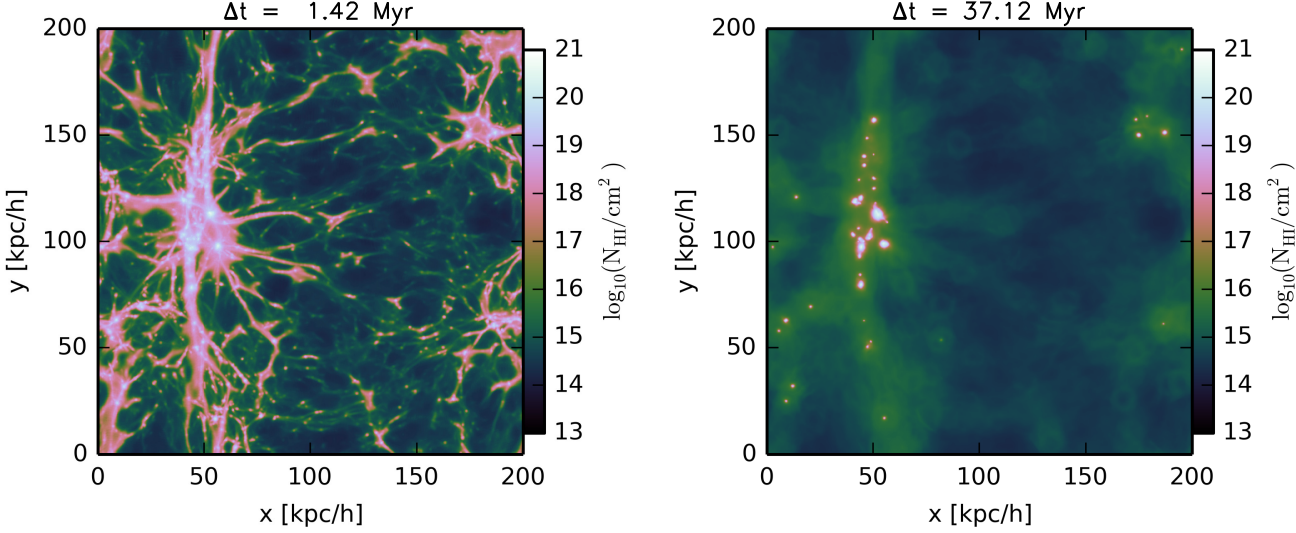


FIG. 11.— The projected H I column density of M\_I-1\_z10 at  $\Delta t = 1.4$  Myr (left) and 37 Myr (right).

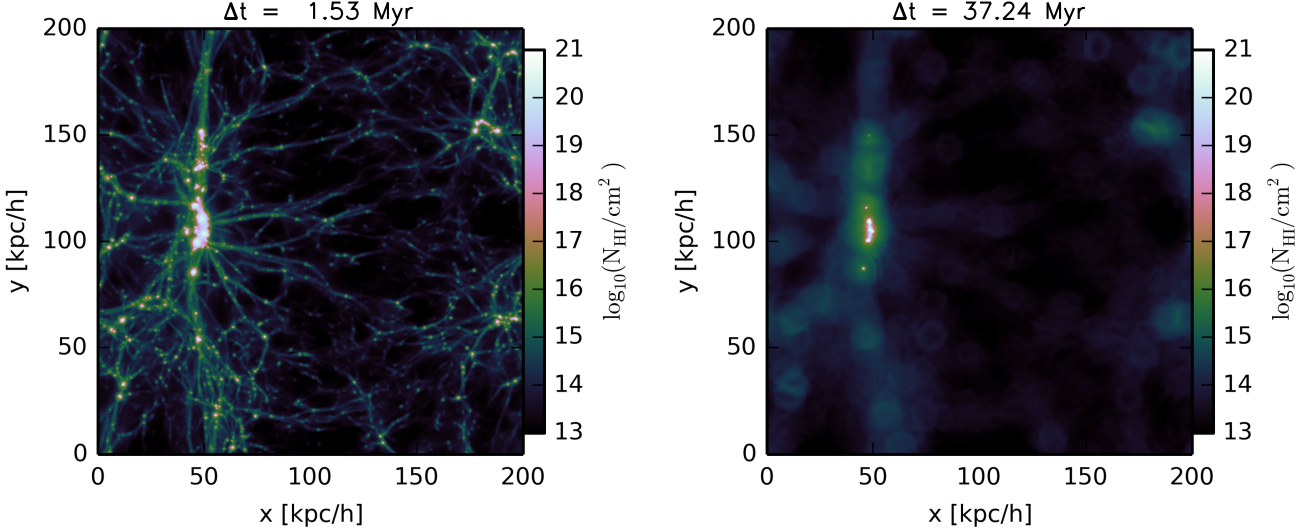


FIG. 12.— The projected H I column density of M\_I0\_z8 at  $\Delta t = 1.5$  Myr (left) and 37 Myr (right).

for lower  $z_i$  and higher  $J_{21}$  with the scaling relation  $N_{\text{rec},150}^{\text{add}} \approx 0.32 \times (J_{21})^{0.12} [(1 + z_i)/11]^{-1.7}$ . Given that 2 - 3 per H atom is often quoted for average the recombination count during the whole reionization era, this level of extra recombination can affect the photon count by more than 10% level. Especially for reionization models that ionize most of its volume toward the end of the EoR (e.g., a model from Iliev et al. (2014)), we can expect up to about 0.7 additional recombination extrapolating from the scaling relation.

It is insightful to look into  $N_{\text{rec},150}^{\text{add}}$  of individual SPH particles in relation to this finding. In the upper panels of Figures 15a, 15b, 15c, and 15d, we scatter-plot  $N_{\text{rec},150}^{\text{add}}$  versus the density at the turn-on of the EIBR ( $n_{\text{init}}$ ) for each gas particle for M\_I0\_z10, M\_I-1\_z10, M\_I0\_z8, and M\_I0\_z10\_NS, respectively, where the color shows the density of the particles in the  $N_{\text{rec},150}^{\text{add}} - n_{\text{init}}$  space. Also

shown in the lower panels is  $dN_{\text{rec},150}^{\text{add}}/d\log_{10} n_{\text{init}}$  that describes the contribution to  $N_{\text{rec},150}^{\text{add}}$  from each  $n_{\text{init}}$ .

In all cases,  $n_{\text{init}}$  correlates with  $N_{\text{rec},150}^{\text{add}}$  to some extent. And, the correlation saturates beyond certain densities with an exception in the no-shielding run. For M\_I0\_z10 and M\_I0\_z8, the saturation happens at  $n_{\text{init}} \sim 0.1 \text{ cm}^{-3}$  and, for M\_I-1\_z10, it happens at  $n_{\text{init}} \sim 0.03 \text{ cm}^{-3}$ . The saturation density coincides with where  $n_{\text{crit}}$  settles down after the R-type phase of I-fronts end. According to the density and ionization histories of individual particles in Figure 8, particles below the threshold density will ionize early at the initial density and will expand to reach close to the cosmic mean density. In this regime, particles that started with higher  $n_{\text{init}}$  will have more chance for recombination. In contrast, particles with the density above the threshold experiences expansion down to the threshold within the D-type shock front before getting ionized. Then, they

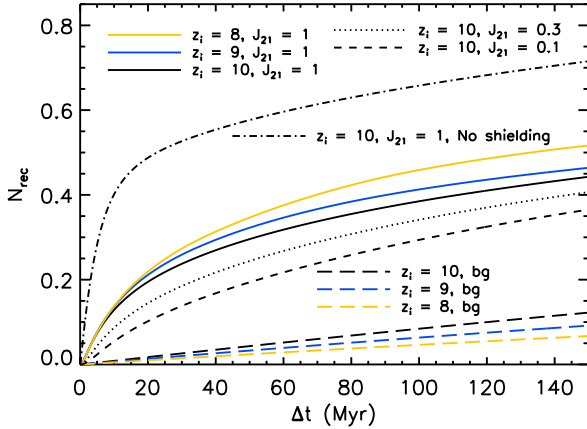


FIG. 13.— The accumulated recombination per  $H$  atom,  $N_{\text{rec}}$ , for M\_I0\_z10 (black solid), M\_I0\_z9 (blue solid), M\_I0\_z8 (yellow solid), M\_I-0.5\_z10 (black dotted), M\_I-1\_z10 (black dashed), and M\_I0\_z10\_NS (black dot-dashed). The black, blue, and yellow long dashed lines describe the background recombination rate calculated from the average gas density and the temperature at each time.

go through density histories similar to those that started just below the threshold density and, hence, experiences similar amounts of recombination. In the no-shielding run, a particle is forced to be ionized instantly at its initial density. Thus, the accumulated recombination keeps increasing for higher initial density without a saturation.

In M\_I0\_z10 and M\_I0\_z8, the  $N_{\text{rec},150}^{\text{add}} - n_{\text{init}}$  relation comes out quite similar in both cases. This is because the characteristics of the EIBR's are similar in those cases.  $N_{\text{rec},150}^{\text{add}} / d \log_{10} n$  in M\_I0\_z8 (lower panel of Fig. 15c) however is greater than in M\_I0\_z10 (lower panel of Fig. 15a) at  $n_{\text{init}} \gtrsim 0.1 \text{ cm}^{-3}$  because more mass is collapsed into that high density range at a lower  $z_i$ . That is, the growth of structure is responsible for the  $(1 + z_i)^{-1.7}$  scaling of  $N_{\text{rec},150}^{\text{add}}$ .

The  $N_{\text{rec},150}^{\text{add}} - n_{\text{init}}$  relation is quite different between M\_I0\_z10 and M\_I-1\_z10. The relation starts similarly from the low-density side in both cases, but it saturates at a lower density in M\_I-1\_z10. The saturation happens at  $n_{\text{init}} \approx 0.2 \text{ cm}^{-3}$  in M\_I0\_z10 whereas it does at  $n_{\text{init}} \approx 0.04 \text{ cm}^{-3}$  in M\_I-1\_z10. As we have discussed above, a lower intensity results in the I-fronts settling down at a lower density. And, a lower saturation density is one aspect of this. The saturation at a lower  $N_{\text{rec},150}^{\text{add}}$  in M\_I-1\_z10 weakens  $N_{\text{rec},150}^{\text{add}} / d \log_{10} n$  above the threshold. This is responsible for the  $(J_{21})^{0.12}$  scaling of  $N_{\text{rec},150}^{\text{add}}$ .

We show  $dN_{\text{rec}}^{\text{add}}/dt$  in the left panel of Figure 14 and fit the result with a 3rd order polynomial in the log-log space as the following.

$$\begin{aligned} \log \left( \frac{dN_{\text{rec}}^{\text{add}}}{dt} \right) &= a_0 + a_1(\log \Delta t) + a_2(\log \Delta t)^2 \\ &\quad + a_3(\log \Delta t)^3 \quad (\Delta t > 2 \text{ Myr}) \\ &= 0 \quad (\Delta t < 2 \text{ Myr}) \end{aligned} \quad (19)$$

For simplicity of the fitting, we do not fit for  $\Delta t < 2$  Myr

when the recombination rate is rising rapidly in the early time. The recombination during that time can be ignored with a negligible error in the time scale of tens of Myr. The fitted parameters are provided in Table 2 for M\_I0\_z10, M\_I0\_z9, M\_I0\_z8, M\_I-0.5\_z10, and M\_I-1\_z10. The result of the fitting is shown in the right panel of Figure 14.

#### 4.6. Mean Free Path

The mean free path,  $\lambda_{\text{mfp}}$ , can be calculated using projected 2D HI column density maps like those in Figure 5. We first calculate the mean cross-section

$$\bar{\sigma} = \frac{\int_{13.6 \text{ eV}/h_p}^{\infty} \frac{I_{\nu}}{h_p \nu} \sigma_{\nu} d\nu}{\int_{13.6 \text{ eV}/h_p}^{\infty} \frac{I_{\nu}}{h_p \nu} d\nu} = 1.62 \times 10^{-18} \text{ cm}^2, \quad (20)$$

where  $h_p$  is the Planck's constant and  $I_{\nu}$  is the intensity of EIBR. Thus, we can regard the bright colored (pink and white) regions with  $N_{\text{HI}} \gtrsim 10^{18} \text{ cm}^{-2}$  in the column density figures as optically thick to the EIBR. To calculate the transmittivity of the EIBR through the entire simulation volume,  $F_{\text{out}}/F_{\text{in}}$ , we take the average of  $e^{-N_{\text{HI}} \bar{\sigma}}$  within the maps. Then,

$$\lambda_{\text{mfp}} = -\frac{l_{\text{box}}}{\log(F_{\text{out}}/F_{\text{in}})}, \quad (21)$$

where  $l_{\text{box}}$  is the box size of the simulation. We show  $\lambda_{\text{mfp}}$  as a function of time for M\_I0\_z10, M\_I0\_z9, M\_I0\_z8, M\_I-0.5\_z10, M\_I-1\_z10, and M\_I0\_z10\_NS in the left panel of Figure 16. Then, we fit our result up to  $\lambda_{\text{mfp}} = 2 \text{ h}^{-1} \text{ Gpc}$  using

$$\begin{aligned} \log(\lambda_{\text{mfp}}) &= b_0 + b_1(\log \Delta t) \\ &\quad + b_2(\log \Delta t)^2 + b_3(\log \Delta t)^3, \end{aligned} \quad (22)$$

where  $b_0, b_1, b_2$ , and  $b_3$  are provided in Table 2. We do not fit the result for  $\lambda_{\text{mfp}} > 2 \text{ h}^{-1} \text{ Gpc}$  as such a large  $\lambda_{\text{mfp}}$  is practically infinite in usual EoR simulations. Also, our box size ( $200 \text{ h}^{-1} \text{ kpc}$ ) would be not reliable to model  $\lambda_{\text{mfp}}$  in such a large scale. The fitting functions are shown in the right panel of Figure 16.

In all the shielded cases (i.e. except in M\_I0\_z10\_NS),  $\lambda_{\text{mfp}}$  grows monotonically and steeply increasing more than two orders of magnitude from  $\Delta t = 1 \text{ Myr}$  to 100 Myr (See the left panel of Fig. 16). For example,  $\lambda_{\text{mfp}}$  in M\_I0\_z10 is  $30 \text{ h}^{-1} \text{ Mpc}$  at  $\Delta t = 1 \text{ Myr}$ ,  $200 \text{ h}^{-1} \text{ Mpc}$  at  $\Delta t = 10 \text{ Myr}$ , and  $30 \text{ h}^{-1} \text{ Gpc}$  at  $\Delta t = 100 \text{ Myr}$ . Such a rapid evolution of  $\lambda_{\text{mfp}}$  warns on assuming  $\lambda_{\text{mfp}}$  as a constant value.

At  $\Delta t \sim 100 \text{ Myr}$ , a kink shows up in the growth of  $\lambda_{\text{mfp}}$  in M\_I0\_z10 and M\_I0\_z9, after which the growth speed is a lot slower. The kink coincides with the evaporation of the last neutral clump in the simulation. Thus, we interpret the kink as the transition of the main limiter of  $\lambda_{\text{mfp}}$  from the neutral clumps to the trace amount of neutral fraction in the diffuse ionized gas. Compared to M\_I0\_z10\_NS, M\_I0\_z10 starts with much lower  $\lambda_{\text{mfp}}$  because the neutral clumps are limiting  $\lambda_{\text{mfp}}$  on photons. After the kink, M\_I0\_z10 and M\_I0\_z10\_NS have almost identical  $\lambda_{\text{mfp}}$ 's. This kink is also expected to happen in M\_I0\_z8, M\_I-0.5\_z10, and M\_I-1\_z10 as well although it is not seen within 150 Myr of time that we simulated these runs. We suppose this is simply because 150 Myr

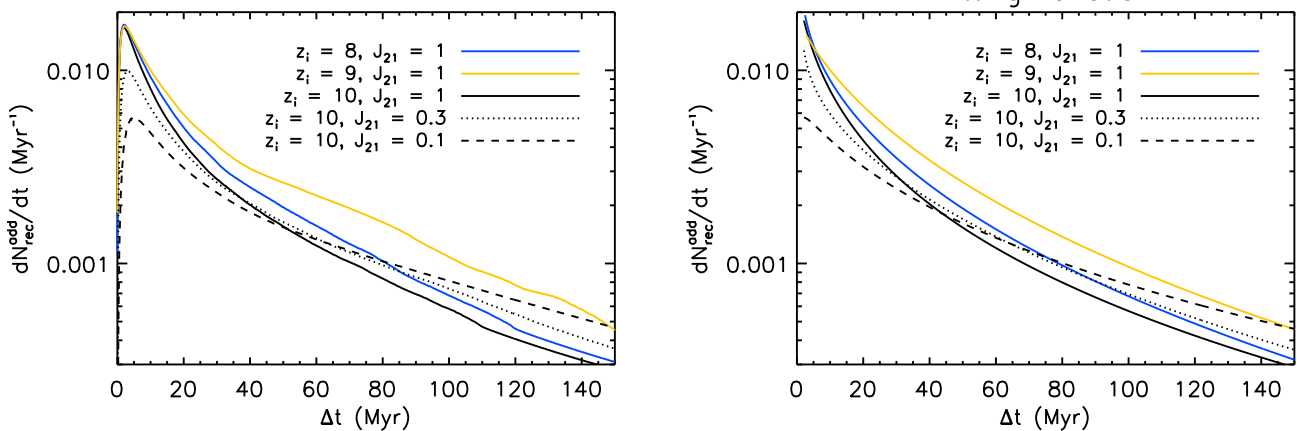


FIG. 14.— (left) The instantaneous recombination count minus the background,  $dN_{\text{rec,add}}/dt$ , plotted for M\_I0\_z10 (black solid), M\_I0\_z9 (blue solid), M\_I0\_z8 (yellow solid), M\_I-0.5\_z10 (black dotted), and M\_I-1\_z10 (black dashed). (right) The fitting functions for the runs shown in the left panel. The line types correspond to the same runs as in the left panel.

is not long enough to finish ionizing all the self-shielded gas in those runs.

The runs with difference  $z_i$ 's and a same  $J_{21}$  (M\_I0\_z10, M\_I0\_z9, & M\_I0\_z8) give the similar evolution trends up to  $\Delta t < 10$  Myr. But, the rise is less steep in the lower  $z_i$  cases after  $\Delta t = 10$  Myr. This is due to the growth structure producing larger clumps that take longer to be evaporated.

In the runs with different  $J_{21}$ 's and a same  $z_i$  (M\_I0\_z10, M\_I-0.5\_z10, & M\_I-1\_z10), the growth speed of  $\lambda_{\text{mfp}}$  is nearly proportional to  $J_{21}$ . For example,  $\lambda_{\text{mfp}}$  exceeds  $100 h^{-1}$  Mpc at around  $\Delta t = 6$  Myr in M\_I0\_z10 whereas it does at  $\Delta t \sim 60$  Myr in M\_I-1\_z10.

##### 5. BOX-SIZE EFFECT

ETA13 reported 1 Mpc as the converging box size for the clumping factor and mean free path. However, the converging box size can be stretched down to 500 kpc given that their clumping factor is shown to be close to converging at that size in Figure 9 of their work. This size however is still about twice bigger than  $200 h^{-1}$  kpc that we adopt as the primary box size of our analysis.

In this work, we test the convergence of our results on the clumping factor and mean free path in box size by creating two cases, S\_I0\_z10 and L\_I0\_z10, that have the same  $z_i$  and  $J_{21}$  as in M\_I0\_z10, but have different box sizes. S\_I0\_z10 is run in a smaller  $100 h^{-1}$  kpc box and L\_I0\_z10 is run in a larger  $400 h^{-1}$  kpc box. Due to the excessive computational expense of L\_I0\_z10, we run it until  $\Delta t = 15$  Myr while the other two cases are run down to  $\Delta t = 150$  Myr.

Figure 3 compares the clumping factors in S\_I0\_z10, M\_I0\_z10, and L\_I0\_z10. S\_I0\_z10 has the clumping factor about 20% smaller than the other two cases do. M\_I0\_z10 and L\_I0\_z10 agree precisely up to  $\Delta t = 2$  Myr, but the clumping factor in L\_I0\_z10 decays more slowly after. The difference grows to  $\sim 10\%$  at  $\Delta t = 15$  Myr. This is difference is made by the number of self-shielded clouds supplying newly ionized dense gas in the late time. The most massive ones in the box should be the ones that are the most effected by the the box size effect in their formation. L\_I0\_z10 is able to keep more self-shielded

clumps that last until late time than M\_I0\_z10 does and this is making difference in the late time clumping factor.  $200 h^{-1}$  kpc seems to be large enough for modeling the clumping factor up to  $\Delta t \sim 1$  Myr, but a larger box is needed to be more precise about the subsequent evolution.

We also expect the box size effect to be an issue for the mean free path. After  $\Delta t = 10$  Myr, only handful of neutral clumps are determining the mean free path of the simulation. For example, we can see in the column density map of M\_I0\_z10 in Figure 5 that we have only six self-shielded clouds setting the mean free path to be  $\sim 1$  Gpc at  $\Delta t = 37$  Myr. In this case, it is unclear that a  $200 h^{-1}$  kpc box would actually represent hundreds of Mpc that the light would go through in the universe.

Given that  $200 h^{-1}$  kpc is well into the nonlinear regime at  $z_i$ 's considered in this work, it is not surprising to have this limitation. But, the qualitative picture about the evolution of structures after ionization should remain valid. Also, having a larger box size would likely to enhance the effects of small-scale structures by allowing more structures to form.

##### 6. SUMMARY AND DISCUSSION

We have presents our results on the clumping factor and mean free path while resolving structures down to the Jeans scale of pre-ionization IGM in the mass and length, aiming to estimate the impact of those structures on ionizing photon budget for reionization and provide sub-grid prescription of recombination rate for large-scale EoR simulations. Our target volume is a sub-Mpc non-star-forming one that is ionized externally by distant ionizing sources. Such volumes act as the sinks of ionizing photons and are much more commons than the sources that host star-forming galaxies.

To achieve this, we have created the GADGET-RT code that fully couples the hydrodynamics to a reasonably accurate prescription for EIBR. This extends the work of ETA13 that used post-processed radiative transfer on top of frozen gas density field. Also, this work is a 3-dimensional extension for the halo evaporation simulations from Shapiro et al. (2004), Iliev et al. (2005b), and

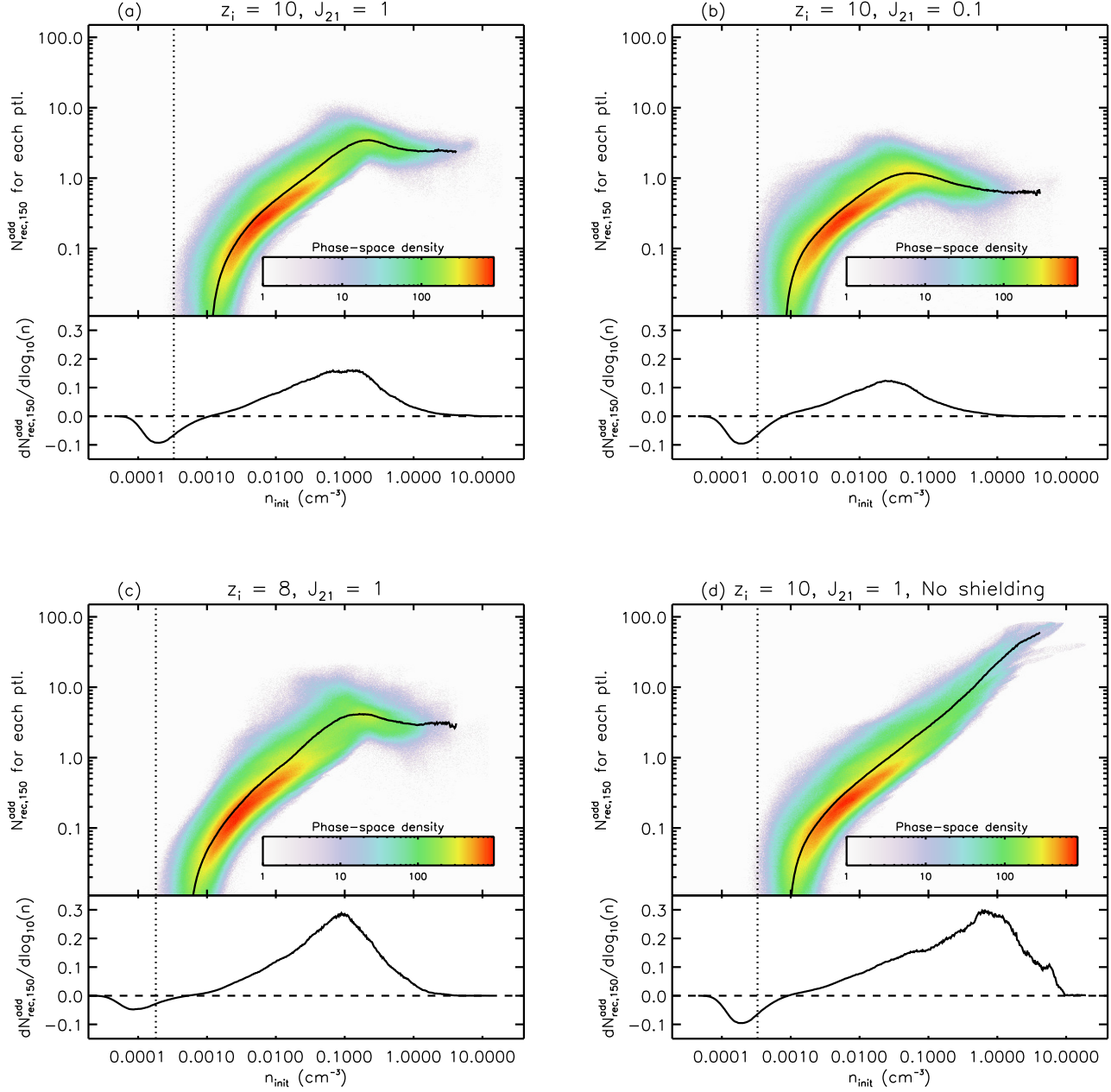


FIG. 15.— Upper panels show the scatter plot of the additional recombination ( $N_{\text{rec},150}^{\text{add}}$ ) versus initial particle density ( $n_{\text{init}}$ ) for M\_I0\_z10 (figure a), M\_I-1\_z10 (figure b), M\_I0\_z8 (figure c), and M\_I0\_z10\_NS (figure d). The vertical dotted line marks the cosmic mean density. Lower panels show  $N_{\text{rec},150}^{\text{add}}/d\log_{10} n$  to describe the contribution to  $N_{\text{rec},150}^{\text{add}}$  from each  $n_{\text{init}}$ . This is obtained by binning and adding up  $N_{\text{rec},150}^{\text{add}}$  of individual particles in the log-space of  $n_{\text{init}}$ .

Ahn & Shapiro (2007). The algorithm has been tested against a well tested code from Ahn & Shapiro (2007) for a spherically symmetric halo evaporation problem. We have run simulations with different  $J_{21}$ 's and  $z_i$ 's to explore the dependence of the clumping factor on these parameters. In the following, we summarize our main findings.

**Evolution of the clumping factor:** When EIBR arrives on small-scale structures, R-type I-fronts starts

sweeping the structures super-sonically from low density regions. This goes on for a few megayears and the clumping factor grows to a large ( $> 10$ ) value during this time. This phase comes to an end when the I-fronts reach dense regions and are converted to D-type. Then, the hydrodynamic feedback on ionized gas destroy the structures in  $\sim 10 - 100$  Myr, causing the clumping factor to decay toward unity.

**Photon budget for the preionization IGM:** The

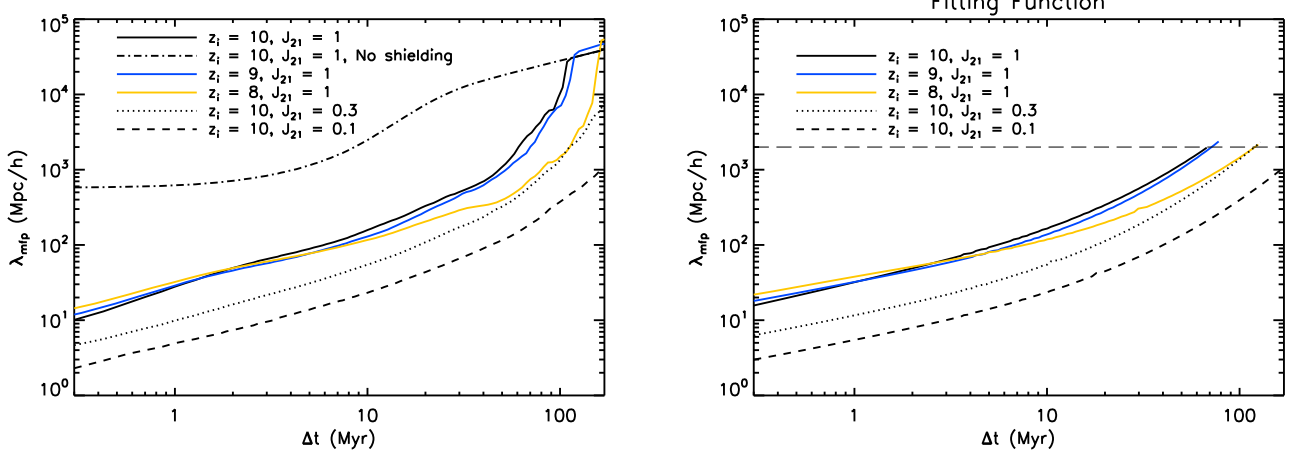


FIG. 16.— (left) The mean free path plotted as a function of  $\Delta t$  for M\_I0\_z10 (black solid), M\_I0\_z9 (blue solid), M\_I0\_z8 (yellow solid), M\_I-0.5\_z10 (black dotted), M\_I-1\_z10 (black dashed), and M\_I0\_z10\_NS (black dot-dashed). (right) The fitting functions for the mean free path. Lines types correspond to the same runs as in the left panel. The thin long-dashed line denotes the mean free path limit, above which we do not fit.

TABLE 2  
FITTING PARAMETERS FOR  $dN_{\text{rec}}^{\text{add}}/dt$  AND  $\lambda_{\text{mfp}}$

label	$z_i$	$J_{21} (\Gamma_{-12})$	$a_0$	$a_1$	$a_2$	$a_3$	$b_0$	$b_1$	$b_2$	$b_3$
M_I0_z10	10	1 (9.2)	-3.8	-0.18	-0.097	-0.0078	3.4	0.70	-0.047	0.027
M_I-0.5_z10	10	0.3 (2.8)	-3.9	-0.67	0.14	-0.034	2.37	0.61	-0.023	0.025
M_I-1_z10	10	0.1 (0.92)	-5.2	0.094	-0.056	-0.012	1.6	0.60	-0.028	0.021
M_I0_z9	9	1 (9.2)	-3.5	-0.56	0.079	-0.030	3.38	0.59	-0.044	0.031
M_I0_z8	8	1 (9.2)	-4.0	-0.16	0.019	-0.027	3.5	0.57	-0.087	0.030

boost in the clumping factor shortly after ionization leaves a significant impact on the recombination accumulated over time. The resulting extra recombinations due to the small-scale structures on top of what is expected from gas at the mean density is given by  $0.32[J_{21}]^{0.12} [(1 + z_i)/11]^{-1.7}$ .

**Mean free path of H-ionizing photons:** The mean free path grows rapidly, cautioning about using it as a constant value. When structures are ionized later, more self-shielded clumps exist to keep the mean free path shorter. When the intensity of EIBR is higher, self-shielded clumps are evaporated faster, leading to more rapid growth of the mean free path.

It is quite meaningful to confirm that the clumping factor peaks at values comparable to those found in simulations without hydrodynamics (e.g., ETA13), and the peak value contributes significantly to the total recombination count even in the presence of the hydrodynamic feedback strongly suppressing small-scale clumpiness. For models in which most of the volume is ionized toward the end of reionization ( $z \sim 6$ ), the photon budget for the preionization IGM can be as large as  $\sim 0.7$  per H atom, which is a substantial amount given that  $\sim 2 - 3$  is often considered in the literature.

As discussed in Section 5, our results are not free from the finite box size effect. This includes the cosmic variance in EIBR, minihalo population, and even the density environment itself. For example, Ahn et al. (2015) show that the population of minihalos has huge variation due

to the variance in the local density environment. Subsequent studies need to follow this up to improve the results quantitatively. Despite the box size effect, findings on the impact of small-scale structures should remain valid on the qualitative level. Taking account of the matter density inhomogeneity on scales larger than that of our sub-Mpc simulation volumes would allow more structures to form and result in a larger impact from the structures.

The isotropy of ionizing background is a powerful assumption that has simplified the shielding algorithm enough for us to actualize the idea of coupling photoionization with the hydrodynamics. Yet, one needs to be careful about interpreting the results as the angular distribution of incoming radiation would be more complex in reality. When a sub-volume is first exposed to the ionizing background, it is likely that a large-scale I-front would be sweeping the entire volume uni-directionally from one side. The radiation would isotropize later as the volume is exposed to ionizing sources from more and more diverse directions. In the early time when the radiation is close to being uni-directional, the geometry of H II regions in reality might differ from what we see in our simulation. However, we note that the details of how early R-type I-fronts go is rather unimportant for the recombination accumulated in the time scales of  $\sim 10$  Myr or longer. Whichever direction the R-type I-fronts sweep across the box, they will end up at density peaks and transition to D-type. At this point, the intensity of the radiation will determine up to what density the gas would be ionized. And, the subsequent hydrody-

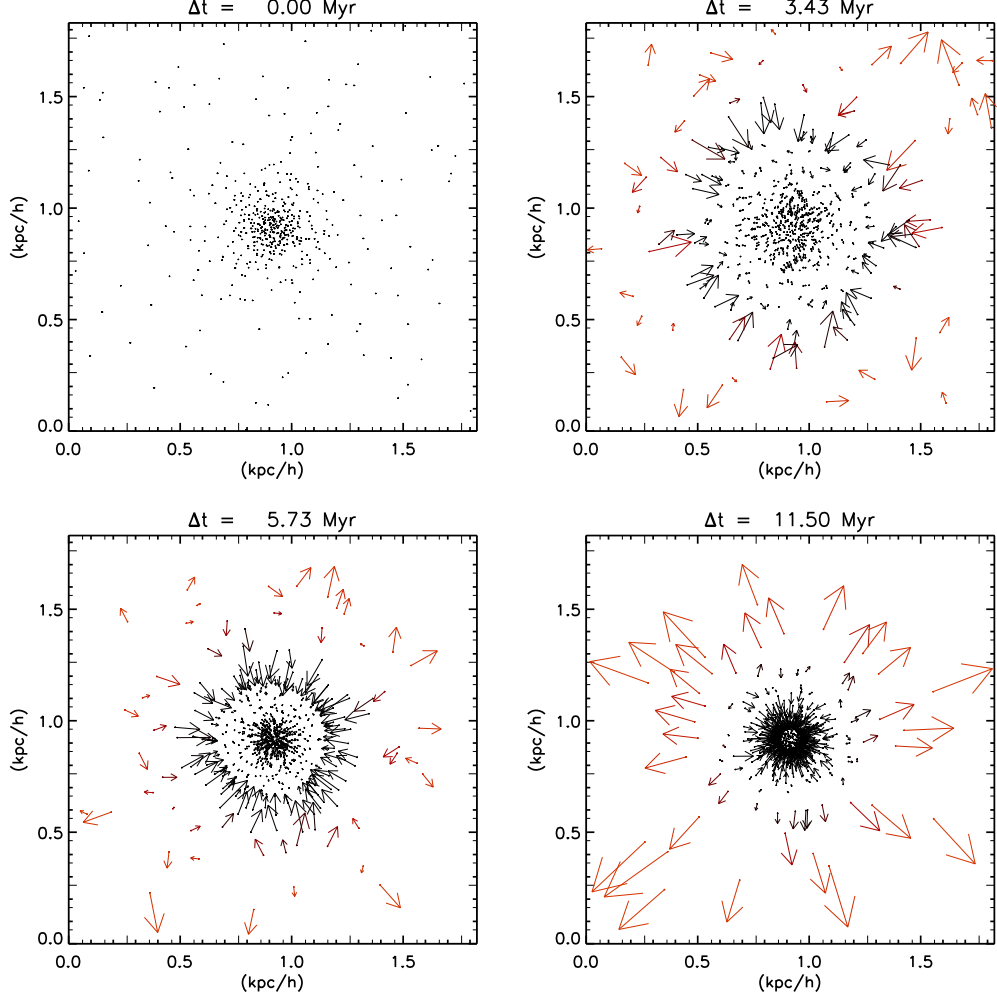


FIG. 17.— SPH particle map of the GADGET-RT simulation at  $\Delta t = 0$  (upper left), 3.43 (upper right), 5.73 (lower left), and 11.5 Myr (lower right). The map samples particles in a plain that goes through the center of the halo and the thickness is 0.2% of the simulation box ( $18.2 h^{-1}$  kpc comoving). Only 20% of the particles are displayed for visual convenience. The arrows denote the projected particle velocities with the positions of their heads giving the linearly extrapolated positions after 5 Myr. Color is used to describe the ionization status of the particle (red-ionized, black-neutral).

namics feedback would make the gas expand from the density peaks that has nothing to do with the direction of EIBR. Here shadows behind self-shielded clumps in the uni-directional case make some difference by leaving some low density gas neutral. But, the column density maps (e.g., Fig. 5) show that the shielded (white and pink) part of the volume is only a tiny fraction, suggesting that it is no so significant.

## 7. ACKNOWLEDGEMENT

Authors thank S. Finkelstein, M. Milosavljevic, E. Komatsu, E. L. Robinson, and M. Alvarez for their

helpful comments on this work. This material is based upon project supported by the National Science Foundation under Grant No. SP13041. PRS was supported in part by U.S. NSF grant AST-1009799, NASA grant NNX11AE09G, NASA/JPL grant RSA Nos. 1492788 and 1515294, and supercomputer resources from NSF XSEDE grant TG-AST090005 and the Texas Advanced Computing Center (TACC) at the University of Texas at Austin. K.A. was supported by NRF-2012K1A3A7A03049606 and NRF-2014R1A1A2059811.

## APPENDIX

### TEST PROBLEM : EVAPORATION OF A SPHERICAL HALO

We test the accuracy of the GADGET-RT code for a spherically symmetric configuration that the one-dimensional radiation-hydrodynamics code of Ahn & Shapiro (2007) can reproduce. In Ahn & Shapiro (2007), the 1D code was used to assess the effects of EIBR on a minihalo with the minimum-energy truncated isothermal sphere (TIS) profile (Shapiro et al. 1999; Iliev & Shapiro 2001). The 1D code accurately captures the evolution of I-fronts both in the supersonic R-type and the subsonic D-type phases. The 1D code has been tested for a number of problems with existing analytical solutions (See Appendix C of Ahn & Shapiro 2007).

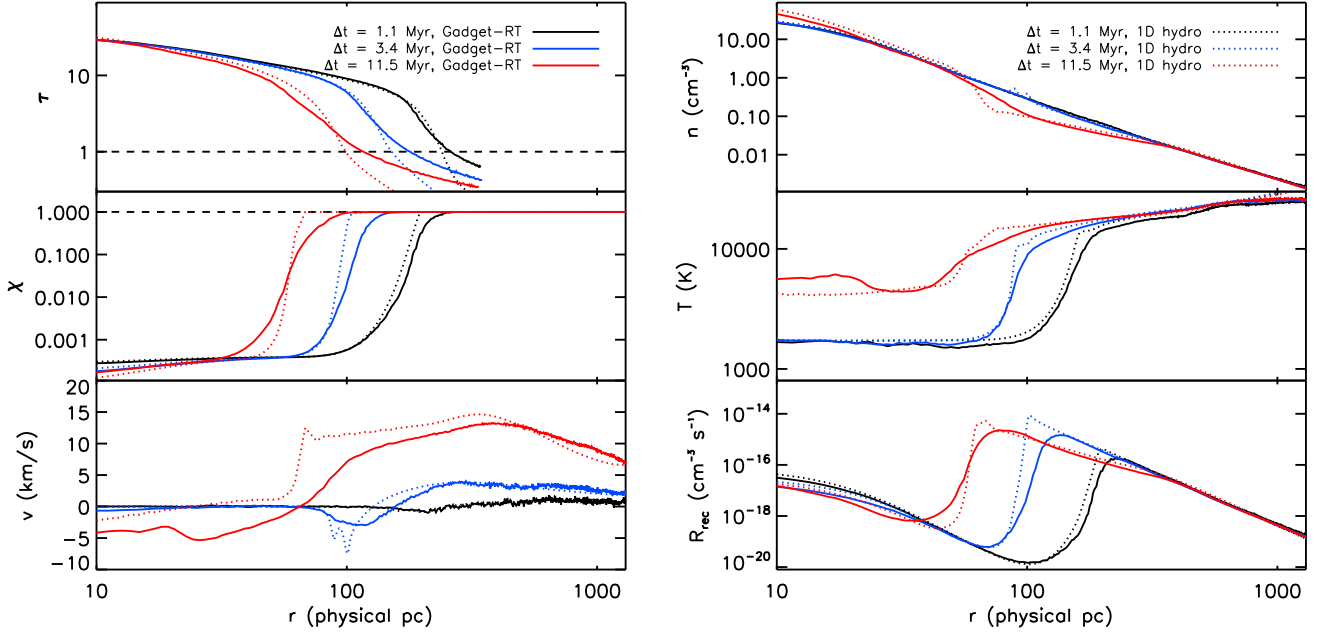


FIG. 18.— Radial profiles of the effective optical depth (top left panel), ionization fraction (middle left panel), radial velocity (bottom left panel), density (top right panel), gas temperature (middle left panel), and recombination rate (bottom right panel) from GADGET-RT of this work (solid) and the 1D radiation-hydro code of Ahn & Shapiro 2007 (dotted). The results are compared for  $\Delta t = 1.1$  Myr (black), 3.4 Myr (blue), and 11.5 Myr (red). The radius on the  $x$ -axis is in the *physical* unit.

We first create the initial conditions for the 1D code using the fitting formula in Appendix A of Shapiro et al. (1999). We adopt  $M = 10^6 M_\odot$  for the mass inside the truncation radius,  $r_t = 170$  *physical pc*, and  $z_{\text{col}} = 10$  for the redshift of collapse. We do *not* truncate the initial density profile at  $r = r_t$ , but instead extend it to  $r = 10r_t$  extrapolating the fitting formula. This extended TIS profile decays toward large- $r$  direction in a reasonable way, allowing us to test the code for the outskirt of the minihalo. The density profile at  $\Delta t = 1.1$  Myr shown in Figure 18 is close to the initial conditions. We keep track of  $N_{\text{sh}} = 10,000$  radial shells linearly spaced from  $r = 10^{-3} r_t$  to  $10 r_t$ . This is the same spatial resolution adopted in Ahn & Shapiro (2007). We bound the outer-most shell with the pressure of that shell at the initial time-step. This pressure becomes practically negligible as soon as the ionization of outer shells photo-heats the gas above 10,000 K from  $\sim 2,000$  K.

We then create the corresponding initial conditions for the GADGET-RT code. We set the box size to be  $20r_t$  and put the center of the halo at the center of the box. We randomly place particles using the extended TIS density profile as the probability function both for the dark matter and gas particles. The effective pressure for the dark matter is converted into the random velocity dispersion following the Boltzmann distribution.

In the 1D code, the optical depth to the background radiation at the  $i$ th shell from the center at the frequency  $\nu$  is given by the angular average over the lines of sight,  $\vec{l}$ :

$$\tau_{\nu,i} = (4\pi)^{-1} \int d\Omega \int_{l=0}^{l_{\max}} dl \sum_X n_{X,j}(r) \sigma_{X,\nu}, \quad (\text{A1})$$

where  $dr$  is the thickness of the shell,  $n_X$  is the number density of a species  $X$ ,  $\sigma_{X,\nu}$  is the cross-section of the species  $X$  for the frequency  $\nu$ , and the baryonic species  $X$  include H, He,  $\text{He}^+$ ,  $\text{H}^-$ ,  $\text{H}_2$ , and  $\text{H}_2^+$ . Here  $l_{\max}$  is the distance from the  $i$ th shell to the outer-most shell.  $r$  is given by

$$r = \sqrt{r_i^2 + l^2 + 2lr_i\mu}, \quad (\text{A2})$$

where  $\mu = \hat{l} \cdot \hat{r}$ . Solving Equation (A2) for  $l$  setting  $r = r_{N_{\text{sh}}}$  gives  $l_{\max}$ .

Since the angular integral in Equation (A3) is symmetric for the azimuthal direction, it can be simplified as the following.

$$\tau_{\nu,i} = \frac{1}{2} \int_{-1}^1 d\mu \int_{l=0}^{l_{\max}} dl \sum_X n_{X,j}(r) \sigma_{X,\nu}. \quad (\text{A3})$$

We use interpolation to define  $n_X(r)$  for  $r_1 < r < r_{N_{\text{sh}}}$ . And, we use the Simpson's Rule to evaluate integrals. For EIBR, we adopt the same parameters used in the standard run (M\\_J0\\_z10) that the spectrum is given by 10<sup>5</sup> K blackbody spectrum and  $J_{21} = 1$ .

Figure 17 shows the particle maps with the velocities and ionization statuses of the particles in the GADGET-RT simulation shown for four snapshots at  $\Delta t = 0$  (upper left panel), 3.43 (upper right panel), 5.73 (lower left panel), and 11.5 Myr (lower right panel). At  $\Delta t > 0$ , the transition between the region populated with black arrows and that populated with red arrows marks an I-front propagating toward the minihalo center. A ring of black arrows pointing toward the center marks a shock that formed in reaction to the increased pressure at the outskirt of the halo. At  $\Delta t = 11.5$  Myr, an out-flow of gas is also observed. These phenomena are all consistent with findings in Ahn & Shapiro (2007).

For quantitative comparison, we compare the radial profiles of six physical quantities from the two simulations in Figure 18. The effective optical depth,  $\tau_{\text{eff}}$ , in the top right panel is defined by  $\tau_{\text{eff}} = -\log(\mathcal{T})$  where  $\mathcal{T} = (1/6)\sum_{x=\pm x, y, z} \exp(-N_x \sigma)$  is the average transmittivity from the six column densities for  $\pm x$ ,  $\pm y$ , and  $\pm z$  directions calculated in the simulation. For the 1D code, the effective optical depth can be calculated precisely from the neutral hydrogen density profile. Along with  $\tau_{\text{eff}}$ , we also compare the radial profiles of the ionized fraction, radial velocity, density, temperature, and recombination rate.

$\tau_{\text{eff}}$  is slightly overestimated in the outer part of the minihalo. This is because the cloud of neutral gas in the minihalo saturate at least one of the six sky pixels in the perspective of a shielded particle with H I column density, making it completely optically thick to the EIBR even when the minihalo is quite distant and should cover less of the sky than that pixel does. This however requires the location of the shielded particle to be not only outside of the cloud, but away from it by a few time the size of the cloud. That is well behind the I-front populated by highly ionized gas, where the overestimation of  $\tau_{\text{eff}}$  does not make any significant error.

For this reason, we generally find a good agreement between the two codes for quantities other than  $\tau_{\text{eff}}$ . Transition zones of the quantities at the I-front tend to be more spread in the GADGET-RT code because the resolution of the GADGET-RT code is unable to perfectly resolve the sharp I-front as in the 1D code. However, the outer fully ionized part of the halo shows an excellent agreement for all the quantities. For the purpose of looking into the fate of ionized gas behind I-fronts, these test results guarantee the reliability of the GADGET-RT code.

## REFERENCES

Ahn, K., Iliev, I. T., Shapiro, P. R., et al. 2012, *ApJ*, 756, L16  
 Ahn, K., Iliev, I. T., Shapiro, P. R., & Srisawat, C. 2015, *MNRAS*, 450, 1486  
 Ahn, K., & Shapiro, P. R. 2007, *MNRAS*, 375, 881  
 Ali, Z. S., Parsons, A. R., Zheng, H., et al. 2015, *ApJ*, 809, 61  
 Alvarez, M. A., & Abel, T. 2012, *ApJ*, 747, 126  
 Asad, K. M. B., Koopmans, L. V. E., Jelić, V., et al. 2015, *MNRAS*, 451, 3709  
 Barkana, R., & Loeb, A. 2004, *ApJ*, 609, 474  
 Bauer, A., Springel, V., Vogelsberger, M., et al. 2015, *MNRAS*, 453, 3593  
 Choudhury, T. R., Haehnelt, M. G., & Regan, J. 2009, *MNRAS*, 394, 960  
 Ciardi, B., Bolton, J. S., Maselli, A., & Graziani, L. 2012, *MNRAS*, 423, 558  
 Clark, P. C., Glover, S. C. O., & Klessen, R. S. 2012, *MNRAS*, 420, 745  
 Crociani, D., Mesinger, A., Moscardini, L., & Furlanetto, S. 2011, *MNRAS*, 411, 289  
 Emberson, J. D., Thomas, R. M., & Alvarez, M. A. 2013, *ApJ*, 763, 146  
 Fan, X., Strauss, M. A., Becker, R. H., et al. 2006, *AJ*, 132, 117  
 Finlator, K., Oh, S. P., Özel, F., & Davé, R. 2012, *MNRAS*, 427, 2464  
 Furlanetto, S. R., Zaldarriaga, M., & Hernquist, L. 2004, *ApJ*, 613, 1  
 Galli, D., & Palla, F. 2013, *ARA&A*, 51, 163  
 George, E. M., Reichardt, C. L., Aird, K. A., et al. 2015, *ApJ*, 799, 177  
 Gnedin, N. Y., & Fan, X. 2006, *ApJ*, 648, 1  
 Gnedin, N. Y., & Ostriker, J. P. 1997, *ApJ*, 486, 581  
 Górski, K. M., Hivon, E., Banday, A. J., et al. 2005, *ApJ*, 622, 759  
 Hahn, O., & Abel, T. 2011, *MNRAS*, 415, 2101  
 Haiman, Z., Abel, T., & Madau, P. 2001, *ApJ*, 551, 599  
 Hirano, S., Hosokawa, T., Yoshida, N., Omukai, K., & Yorke, H. W. 2015, *MNRAS*, 448, 568  
 Iliev, I. T., Mellem, G., Ahn, K., et al. 2014, *MNRAS*, 439, 725  
 Iliev, I. T., Scannapieco, E., & Shapiro, P. R. 2005a, *ApJ*, 624, 491  
 Iliev, I. T., & Shapiro, P. R. 2001, *MNRAS*, 325, 468  
 Iliev, I. T., Shapiro, P. R., & Raga, A. C. 2005b, *MNRAS*, 361, 405  
 Kaurov, A. A., & Gnedin, N. Y. 2015, *ApJ*, 810, 154  
 Krug, H. B., Veilleux, S., Tilvi, V., et al. 2012, *ApJ*, 745, 122  
 Madau, P., Haardt, F., & Rees, M. J. 1999, *ApJ*, 514, 648  
 Miralda-Escudé, J. 2003, *ApJ*, 597, 66  
 Miralda-Escudé, J., Haehnelt, M., & Rees, M. J. 2000, *ApJ*, 530, 1  
 Paciga, G., Albert, J. G., Bandura, K., et al. 2013, *MNRAS*, 433, 639  
 Pawlik, A. H., Schaye, J., & van Scherpenzeel, E. 2009, *MNRAS*, 394, 1812  
 Planck Collaboration, Ade, P. A. R., Aghanim, N., et al. 2014, *A&A*, 571, A16  
 Prochaska, J. X., O'Meara, J. M., Fumagalli, M., Bernstein, R. A., & Burles, S. M. 2015, *ApJS*, 221, 2  
 Prochaska, J. X., O'Meara, J. M., & Worseck, G. 2010, *ApJ*, 718, 392  
 Raičević, M., & Theuns, T. 2011, *MNRAS*, 412, L16  
 Robertson, B. E., Ellis, R. S., Dunlop, J. S., McLure, R. J., & Stark, D. P. 2010, *Nature*, 468, 49  
 Shapiro, P. R., Iliev, I. T., & Raga, A. C. 1999, *MNRAS*, 307, 203  
 —. 2004, *MNRAS*, 348, 753  
 Shukla, H., Mellem, G., Iliev, I. T., & Shapiro, P. R. 2016, *MNRAS*, arXiv:1602.01144  
 Shull, J. M., Harness, A., Trenti, M., & Smith, B. D. 2012, *ApJ*, 747, 100  
 So, G. C., Norman, M. L., Reynolds, D. R., & Wise, J. H. 2014, *ApJ*, 789, 149  
 Songaila, A., & Cowie, L. L. 2010, *ApJ*, 721, 1448  
 Springel, V. 2005, *MNRAS*, 364, 1105  
 Springel, V., White, S. D. M., Tormen, G., & Kauffmann, G. 2001, *MNRAS*, 328, 726  
 Storrie-Lombardi, L. J., McMahon, R. G., Irwin, M. J., & Hazard, C. 1994, *ApJ*, 427, L13  
 Trac, H., & Cen, R. 2007, *ApJ*, 671, 1  
 Yoshida, N., Oh, S. P., Kitayama, T., & Hernquist, L. 2007, *ApJ*, 663, 687  
 Yoshida, N., Oh, S. P., Hernquist, L., & Abel, T. 2006, *ApJ*, 652, 6